Icarus 388 (2022) 115216

Contents lists available at ScienceDirect

Icarus

journal homepage: www.elsevier.com/locate/icarus

New interpretations of lunar mare basalt flow emplacement from XCT analysis of Apollo samples

Aleksandra J. Gawronska [a,*], Claire L. McLeod [a], Erika H. Blumenfeld [b,c,1], Romy D. Hanna [d], Ryan A. Zeigler [e]

[a] Department of Geology and Environmental Earth Science, Miami University, Oxford, OH 45056, United States of America
[b] Independent Transdisciplinary Artist
[c] LZ Technology, JETS Contract, NASA Johnson Space Center, Houston, TX 77058, United States of America
[d] Jackson School of Geosciences, University of Texas at Austin, Austin, TX 78712, United States of America
[e] NASA Johnson Space Center, Houston, TX 77058, United States of America

ARTICLE INFO

Keywords:
Volcanism
Geological processes
Moon
Surface

ABSTRACT

The study of basaltic samples returned half a century ago through the Apollo missions has provided unparalleled insights into the magmatic processes associated with volcanism on planetary bodies. Traditional study of these samples has been conducted in two dimensions (2D) via interrogation of thin sections and subsequent in-situ chemical analyses, yet returned samples are three-dimensional (3D) objects and therefore preserve evidence of lunar volcanic processes in 3D. Here, X-ray computed tomography (XCT) was used for the first time to evaluate lava emplacement mechanisms on the lunar surface. A total of six samples from the Apollo 11, 12, 15, and 17 missions were studied. From volumetric mineralogies, textures, and petrofabrics, lunar lava cooling histories were inferred. Collectively, these physical characteristics were then correlated with pāhoehoe lava flow lobe stratigraphy. Samples 10057 and 15556 are inferred to have crystallized in the lobe crust of their respective lava flow lobes. Samples 12038, 12043, and 70017 may mark the transition between the vesiculated, fine-grained lobe crust, and the dense, coarse-grained lobe core in their respective flows. Finally, coarse-grained, and non-vesiculated sample 15085 is inferred to have crystallized in a lobe core. No statistically significant petrofabric is preserved in any of the samples, indicating that the basalt samples studied here, and the lava flows they originated from, experienced minimal strain during emplacement and solidification on the lunar surface. This is consistent with the low viscosities attributed to lunar mare lavas. Future in-situ sampling of extraterrestrial basaltic products should focus on detailed documentation of, and collection from, stratigraphically well-characterized lava flows to further evaluate the interpretations presented here.

1. Introduction

Magmatism is a fundamental process through which rocky objects across our Solar System differentiate and evolve (BVSP, 1981; Wilson and Head, 2018). The Earth's Moon is one of the most comprehensively characterized extraterrestrial objects in our Solar System as a result of over half a century's worth of scientific investigation. This includes insights from remote sensing (e.g., Gillis et al., 2003, 2004; Lemelin et al., 2019), in-situ sample return during the Apollo, Luna, and Chang'e 5 missions (e.g., Heiken et al., 1991; Li et al., 2021a; Papike et al., 1976; Qian et al., 2021; Taylor, 1982), and the discovery of lunar meteorites on Earth (e.g., Allan Hills 81005, Brum et al., 2020; Gross and Treiman, 2011; Treiman and Drake, 1983). Following in-situ sample return, and the identification of basaltic material in lunar meteorites, numerous studies have worked to characterize the microstructural and geochemical diversity that exists within lunar basaltic products (e.g., glassy to microgabbroic textures, Kramer et al., 1977; Ryder, 1985, 1993; Warner, 1970; characteristic Ti, K, and Al contents, Neal and Taylor, 1992, and references therein). As a result, our understanding of lunar basalt petrogeneses and the magmatic processes which operate across rocky planetary objects has greatly advanced (Cone et al., 2020; Neal and Taylor, 1992; Shearer et al., 2006). For example, it is now well

* Corresponding author.
E-mail address: gawronaj@miamioh.edu (A.J. Gawronska).
[1] www.erikablumenfeld.com

https://doi.org/10.1016/j.icarus.2022.115216
Received 1 September 2021; Received in revised form 15 July 2022; Accepted 8 August 2022
Available online 15 August 2022
0019-1035/© 2022 Elsevier Inc. All rights reserved.

established that lunar magmas originated from distinct source regions within the lunar mantle and evolved to produce a petrographically and geochemically diverse suite of basalts. However, questions remain regarding the dynamics of lava emplacement onto the lunar surface (e.g., Gregg, 2017; Hamilton, 2019; Tolometti et al., 2020; Wilson, 2009) and how the crystal and vesicle contents of lunar lavas contributed to flow rheology and emplacement mechanisms (Belousov and Belousova, 2018; Bergantz et al., 2017; Lejeune et al., 1999; Nicolas and Ildefonse, 1996; Paterson et al., 2019; Rumpf et al., 2020; Vernon, 2018).

On Earth, basaltic pāhoehoe lava flows are emplaced through the process of inflation (e.g., Belousov and Belousova, 2018; Keszthelyi and Self, 1998; Rowland and Walker, 1988; Self et al., 1998; Wilson, 2009). During inflation, basaltic lava lobes grow and rupture, generating subsequent lobes. Inflating lava lobes quickly develop a glassy crust that works to trap vesicles as magma continues to be injected into the lobe. This often creates vesicle-rich zones in the lobe crust where the vesicles increase in size but decrease in number inward (e.g., Belousov and Belousova, 2018; Cashman and Kauahikaua, 1997; Hon et al., 1994; Keszthelyi and Self, 1998; Self et al., 1998; Vye-Brown et al., 2013; Thordarson, 1995; Wilmoth and Walker, 1993). The remainder of each lobe is comprised of a relatively insulated core, and a quenched crust at the base of the lobe. On Earth, this base is ~ 10 cm thick, irrespective of total lobe thickness (Self et al., 1998). The core of the flow lobe can be vesiculated, but it is often vesicle-poor as bubbles rise towards the crust prior to solidification. Furthermore, magmas with higher crystal contents and lower melt fractions have an increased potential to develop mineral flow textures, particularly when only 35 to 40% melt remains (e.g., Paterson et al., 1998; Vernon, 2018). However, recent work also suggests that petrofabrics resulting from flow can be far more complex than simple parallel alignment of crystals (Paterson et al., 2019, and references therein; Žák et al., 2007).

Due to their mafic natures (namely <52 wt.% SiO_2), terrestrial basalts have relatively low viscosities. From observational and experimental studies, the viscosities of lunar basaltic lavas have been interpreted to be one to two orders of magnitude lower than those on Earth (Harris and Allen, 2008; Keszthelyi and Self, 1998; Murase and McBirney, 1970; Rumpf et al., 2020; Taylor et al., 1991; Whitford-Stark, 1982). These lower viscosities (~ 0.13 to 0.87 Pa-s, Rai et al., 2019) suggest that lunar basaltic eruptions may have had high effusion rates and large volumes (e.g., BVSP, 1981; Garry et al., 2012; Head and Wilson, 1992). However, effusion rates also likely varied regionally and temporally and thus created flows of varying thicknesses (e.g., Rumpf et al., 2020). Based on their low viscosities and picritic compositions, the lunar mare basalts were possibly emplaced as pāhoehoe lava flows, and formed inflated lava lobes (Donohue and Neal, 2015; Garry et al., 2012; Keszthelyi and Self, 1998; Li et al., 2021b; Roberts and Gregg, 2019; Rumpf et al., 2020; Self et al., 1998; Tolometti et al., 2020; Vye-Brown et al., 2013; Wilson, 2009). The Apollo basalts studied here will be discussed within this framework.

The only field-based study of a lava flow outcrop on the lunar surface to date occurred during the Apollo 15 mission, when flows <1 m to 20 m thick were found to be exposed in the side of Hadley Rille (Howard et al., 1972; Howard and Head III, 1972; Swann et al., 1972; Spudis et al., 1988; Vaniman et al., 1991). More recent studies have utilized remote sensing techniques to map lunar flows and investigate their properties (e.g., Head and Wilson, 1992; Hiesinger et al., 2002; Weider et al., 2010; Tolometti et al., 2020). For example, remote work has indicated that several flows are tens to hundreds of meters thick in Mare Tranquilitatis and Humorum (Hiesinger et al., 2002), and in Oceanus Procellarum (Weider et al., 2010). It is, however, challenging to distinguish individual flows from each other within an outcrop from remote sensing alone. The large thicknesses reported by Hiesinger et al. (2002) and Weider et al. (2010) may represent total outcrop thicknesses, and not individual flow thickness (Rumpf et al., 2020; Tolometti et al., 2020; Wilson, 2009). In the absence of lunar field work and in-situ observations of flow characteristics, the work presented here aims to investigate lunar lava flow emplacement via the study of basaltic rock chips from the Apollo 11, 12, 15, and 17 missions.

Advancing our understanding of lunar magmatic systems has historically been supported through traditional petrographic methods and subsequent in-situ analysis of samples in 2D via thin section and/or grain mount study (e.g., through electron microscopy and microanalysis, McCubbin et al., 2019). These traditional techniques require some degree of sample destruction, either by slicing, crushing, and/or dissolving. The relative paucity of lunar, and more broadly extraterrestrial, materials available for scientific study necessitates their investigation via non-destructive techniques. X-ray computed tomography (XCT) is one such approach. XCT is an imaging technique that permits measurement and analysis of a sample (and its components) in 3D, thus providing a more accurate record of lunar materials. XCT also provides a comparatively greater amount of material to study when compared to traditional 2D thin section analysis, and works to facilitate sample preservation and curation (e.g., Blumenfeld et al., 2017, 2019; McCubbin et al., 2015; Zeigler et al., 2021). The utility of XCT to advance our understanding of the properties of various materials has been widely demonstrated in numerous fields over the past several decades, including applications in paleontology (Carvalho et al., 2020; Cunningham et al., 2014; Wu and Schepartz, 2009), economic geology (Arif et al., 2021; Gan et al., 2020; Mathews et al., 2017; Wang and Miller, 2020; Zhang et al., 2019), and materials science (du Plessis and Boshoff, 2019; Vásárhelyi et al., 2020). Within the context of extraterrestrial research, XCT has previously been applied to characterize the petrography, petrofabrics, porosities, and chemistries of chondritic and Martian meteorites in order to improve understanding of their formation and origin (e.g., Hanna and Ketcham, 2017; Hezel et al., 2013). Within the context of lunar science, and at the time of writing, the Apollo Next Generation Sample Analysis program is beginning to undertake XCT analyses on Apollo 17 samples opened in the year 2019 (i.e., Zeigler et al., 2021).

The work presented here is the first to evaluate lunar basalt petrofabrics and lunar eruptive environments in 3D through the application of XCT. Specifically, textures were observed three-dimensionally for each sample and shape preferred orientations were quantified in order to evaluate whether foliation or lineation was preserved. In addition, particle and vesicle size distributions were quantified in order to determine the cooling history of each sample. Collectively, these data were used to interrogate lava flow stratigraphy and evaluate the emplacement history of lava flows across the lunar surface.

2. Methodology

2.1. Sample descriptions

Samples studied as part of this work represent much of the textural and chemical diversity that exists throughout the Apollo basalt suite, and are associated with the Apollo 11 (sample 10057,19–128.7 g), Apollo 12 (sample 12038,7–327.5 g; sample 12043,0–52.4 g), Apollo 15 (sample 15085,0–234.3 g; sample 15556,0–619.2 g), and Apollo 17 (sample 70017,8–1423.2 g) missions. Hereafter, the samples are only referred to by their parent generic number (e.g., 15556).

Previous studies have provided detailed petrographic summaries of each sample (see Table 1; see also Meyer, 2016, and references therein). Sample 10057 is a fine-grained, vesicular, high-potassium ilmenite basalt with intergrown subhedral plagioclase, ilmenite, and pyroxene. Sample 12038 is categorized as a coarse-grained, hypidiomorphic feldspathic basalt where the feldspars form a loose network. Sample 12043 is a medium-grained pigeonite basalt with pyroxene phenocrysts set in a subophitic groundmass. Sample 15085 is a coarse-grained pigeonite basalt dominated by pyroxene. Sample 15556 is a fine-grained, vesicular olivine-normative basalt with pyroxene subophitically enclosing plagioclase and ilmenite grains. Sample 70017 is a medium-grained, hypidiomorphic, granular low-potassium ilmenite basalt. Previous

Table 1
Summary of sample modal mineralogy.

Sample Number	Sample description*	Sample texture*	Oxides†		Pyroxene		Plagioclase feldspar		Others§		Vol% of unassigned voxels#	Total subsample volume (mm^3)
			This study (vol%)	Previous studies*	This study (vol%)	Previous studies*	This study (vol%)	Previous studies*	This study (vol%)	Previous studies*		
10057	High-K ilmenite	Fine-grained, vesicular	19.8	15.5–15.7	49.3	50.8–50.9	30.8	19.2–24	N.A.	3.3	0.04	38,237
12038	Feldspathic	Coarse-grained, equigranular	2.7	3.46–10	63.5	48.8–55	33.8	30–44	N.A.	2.7–3.4	0.003	101,434
12043	Pigeonite	Medium-grained, subophitic	1.2	3.5	76.9	57.7	21.8	32.9	N.A.	4.5	0.02	16,380
15085	Pigeonite	Coarse-grained, ophitic	4.9	3–3.5	62.5	40–66	29.5	22–60	2.99	1.6–2.4	0.2	74,390
15556	Olivine-normative	Fine-grained, subophitic vesicular	1.2	3–8	38.3	50–57	60.5	30–38	N.A.	1.8–6	N.A.	180,768
70017 (full)	Low-K ilmenite	Medium-grained, poikilitic, equigranular	4.7	19.2–22.8	48.2	49.3–57.6	45.4	19.8–26	N.A.	1.6–3	1.7	333,627
70017 (cropped)	Low-K ilmenite	Medium-grained, poikilitic, equigranular	21.5	19.2–22.8	42.0	49.3–57.6	36.5	19.8–26	N.A.	1.6–3	N.A.	139,782

* Data gathered from the Lunar Sample Compendium (Meyer, 2016, and references therein).
† Oxides include ilmenite, spinels, and Fe-metal.
§ Other studies found mesostasis and "silica." Here, it was not possible to separate other sample components except tridymite in 15,085,0.
\# Voxel is a volume element, a 3D pixel.

studies of these samples have also established their modal mineralogies based on 2D thin section analysis (reported in Meyer, 2016, and references therein). Broadly, all samples are comprised of abundant pyroxene and plagioclase feldspar, minor olivine, and trace amounts of accessory phases. Samples 10057 and 70017 are both categorized as high-titanium (~ 10 to 13 wt. % TiO_2) basalts, and thus have abundant ilmenite, whereas the remaining samples contain low bulk wt. % TiO_2 contents (~ 2 to 3 wt. %) and have only accessory ilmenite (see Meyer, 2016, and references therein).

The samples studied here vary in vesicle abundances, distributions, and shapes (i.e., Meyer, 2016, and references therein). Gas cavities that remain in volcanic materials after crystallization and are often, but not always, rounded werecategorized to as vesicles in the work presented here. Relatively small cavities that remain after solidification, are interstitial to crystals, and are bounded by crystal faces were referred to as vugs. Gas cavities that existed prior to solidification were referred to as bubbles.

2.2. Data extraction

Documentation of XCT methodologies used for geologic applications is presented in Cnudde and Boone (2013), Ebel and Rivers (2007), Hanna and Ketcham (2017), and Jerram and Higgins (2007). Five of the six samples studied here were originally scanned as part of the Astromaterials 3D project, a novel effort to create research-grade interior and exterior 3D models of NASA's astromaterials collections for researchers and the public (Blumenfeld et al., 2017). Those five samples (12038, 12043, 15085, 15556, and 70017) were scanned on a North Star Imaging system the University of Texas at Austin High Resolution Computed Tomography Facility (UTCT). The work presented here was selected as a case study for Astromaterials 3D and authors were provided access to the relevant datasets. At the time of writing, three of these samples (12038,7, 15556,0, and 70017,8) can be accessed through the Astromaterials 3D library (https://ares.jsc.nasa.gov/astromaterials3d/). Sample 10057,19 was scanned separately at the Natural History Museum in London, UK on a Nikon Metrology HMX ST 225. Details of the scanning parameters used are summarized in Table S1. Each sample was triple bagged in Teflon for the duration of the scan. As XCT data permit the user to view the sample in more than one direction, sample textures were evaluated while looking down the orthogonal x, y, and z axes (the orthogonal z axis is parallel to the axis of rotation, x and y are the remaining two axes), as shown in Fig. 1. Grayscale values vary depending on X-ray attenuation as a result of differences in chemical composition and material density within each voxel (volume element, i. e., a 3D pixel). *ImageJ* (Schneider et al., 2012) was used to adjust the brightness and contrast of the scans to support phase segmentation efforts. *Dragonfly* (version 2021.1, Object Research Systems (ORS) Inc, 2020) was used to generate masks of the area external to each sample (referred to as the "outside" here) so that this area could be segmented away. Any vesicles connected to the "outside" component could not be quantified and were discarded as well. The original sample scans (with contrast and brightness values adjusted) had a black "outside" – the applied mask was assigned a value of 255 (white). This approach was taken for all samples except 15556,0, where a mask could not be created due to computational limitations and thus the "outside" and vesicles had the same threshold value. In sample 15556 the "outside" and vesicle components were segmented together as one component, and separated later based on blob volumes (described further below).

Segmentation and separation of sample components was completed using *Blob3D* (Ketcham, 2005), a freely available program developed to extract component information from XCT data. Here, "component" was used to indicate mineral phases, while "particle" was used to indicate individual grains of a mineral phase. Sample components included the mineral phases pyroxene (±olivine), plagioclase feldspar, and oxides (includes all of the brightest phases, namely ilmenite with minor Fe-rich spinels, and sulfides), as well as vesicles, and the "outside." This is an oversimplification of the samples' true mineral assemblage, as accessory minerals overlap in grayscale value with major components. For

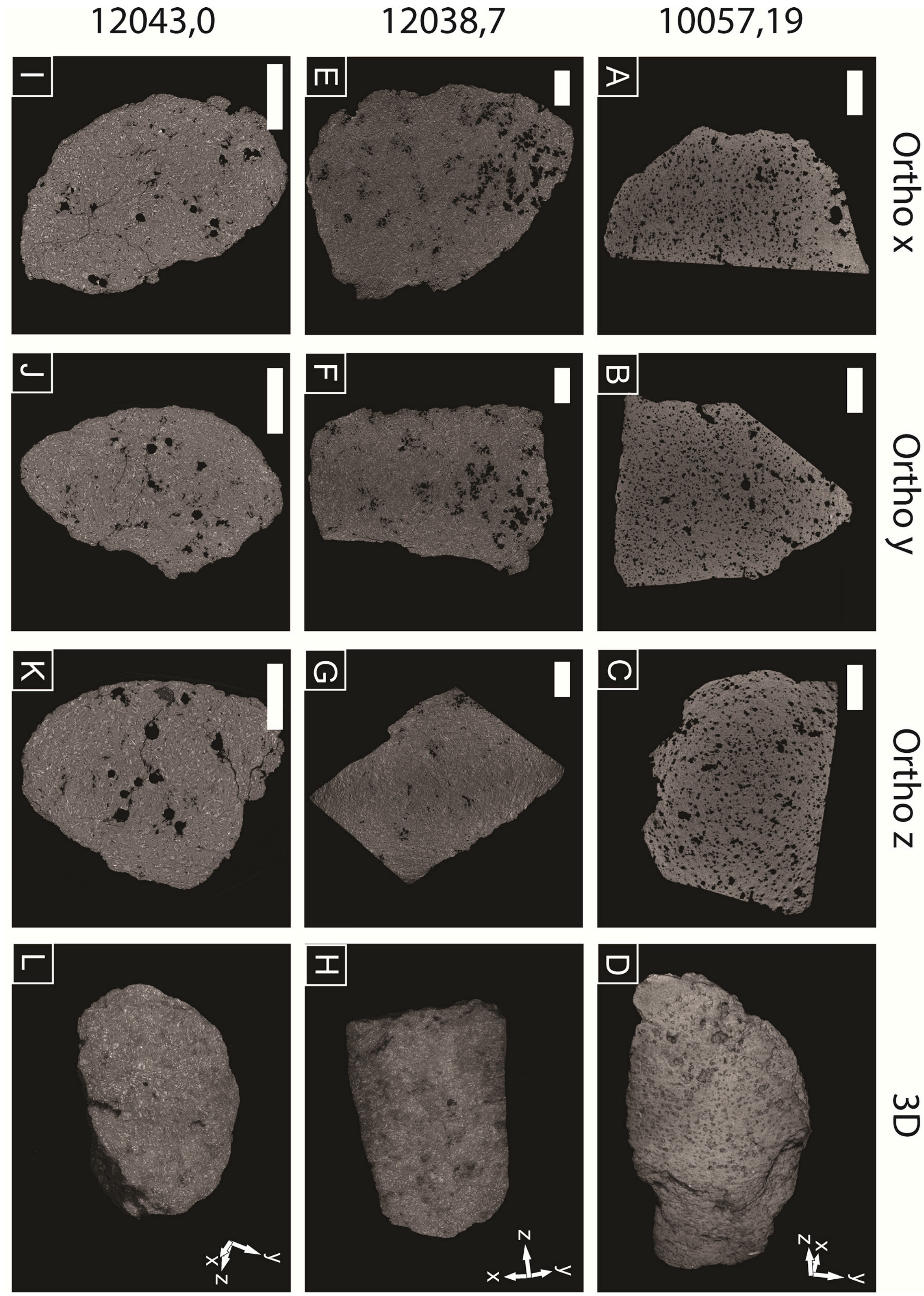

Fig. 1. Scan slices at sample center for each of the samples studied here. Scale bars are 1 cm long. The scans were used to create 3D models of samples using *Dragonfly* (Object Research Systems (ORS) Inc, 2020), seen in panels D, H, L, P, T, and X. Videos of the models can be found in the supplementary materials.

example, the component "plagioclase feldspar" likely included some K-feldspar and glass. When possible, accessory phases were segmented into an additional "other" category. This allowed for the separation of tridymite found in sample 15085 (described further in section 3.1). Olivine was not segmented because it was indistinguishable from pyroxene. Previous authors have indicated that olivine constitutes a minor component in all samples studied here (~ 1%, Meyer, 2016 and references therein). Its presence should therefore not significantly affect the

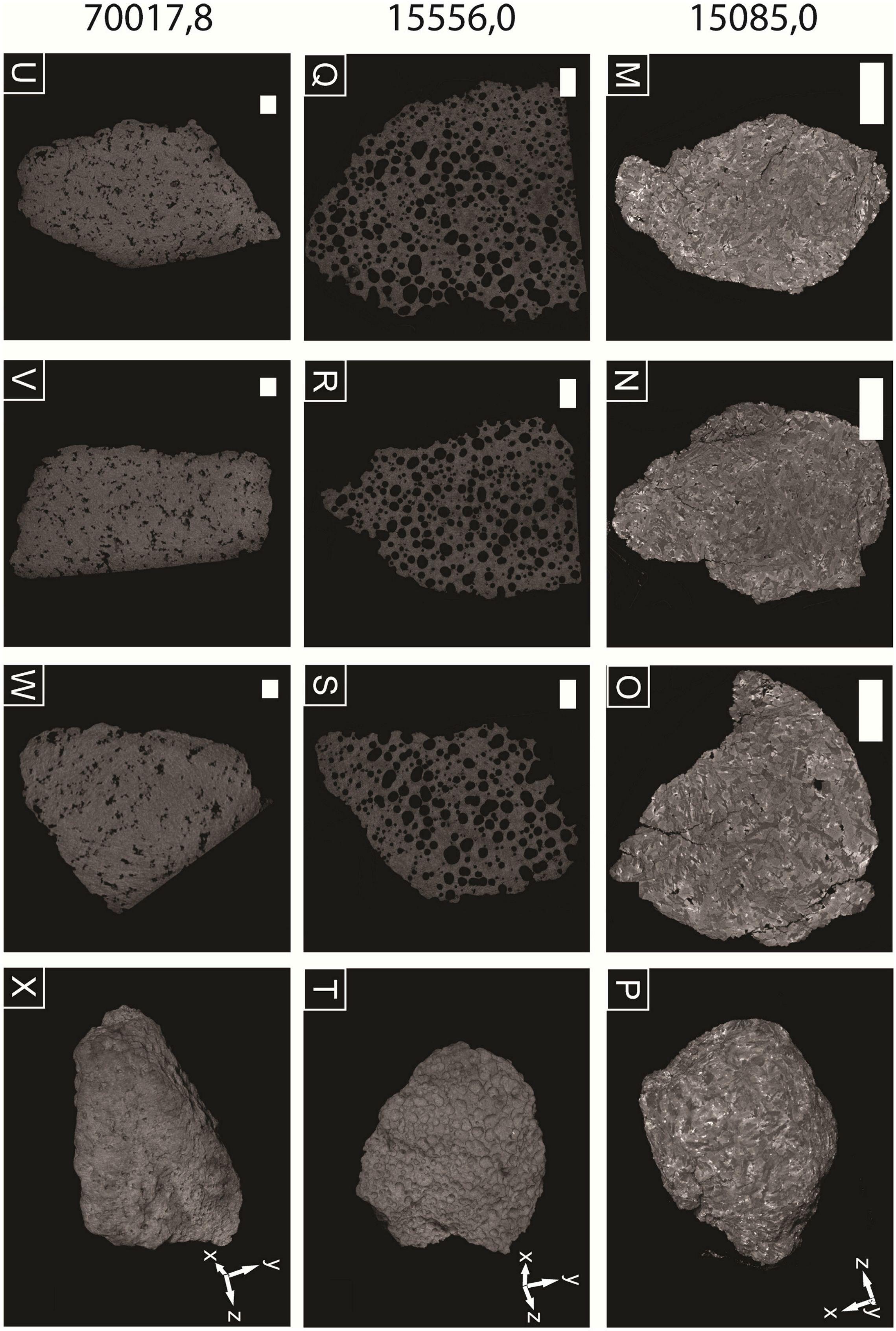

Fig. 1. (*continued*).

pyroxene abundances reported here.

Voxels were segmented into components based on their grayscale values using the general thresholding option in *Blob3D*, where a range of grayscale values was chosen for a component, and only voxels with a value within this range were attributed to the component by *Blob3D* (Fig. 2A-B). Occasionally, seeding was used to specifically dictate to *Blob3D* that voxels of certain a greyscale range may only be included in a component if they are touching a voxel of a specified (seed) value. This helped to differentiate phases that partially overlapped in their grayscale values (e.g., bright iron-rich pyroxene rims and bright Fe- and Ti-rich oxide phases, see Fig. 3). After segmentation, the next step in *Blob3D* was to separate objects within the same component that are touching, so that the program was able to identify and measure them as discrete objects (Fig. 2C).

Throughout the studied sample suite, the majority of pyroxene and feldspar grains were in direct contact with several grains of the same phase. While it may be technically possible to manually separate these grains in *Blob3D*, this approach would have been very time intensive due to each sample containing multiple thousands of grains of each phase. Therefore, we analyzed here only the total volumes of pyroxene and plagioclase, and not the shape-preferred orientations of individual grains or the average range in crystal sizes of each mineral phase. Oxide and vesicle data was separated using "No Separation" where each particle or particle cluster was treated as one. Extracting particle characteristics followed. During extraction, a best-fit ellipsoid was fit to each individual oxide and vesicle particle to extract shape and orientation of these objects with respect to the overall sample. While the individual particles were not necessarily ellipsoidal in shape, this approach worked to characterize their shape-preferred orientation. In order to ensure that the smallest distinguishable particles were accounted for, even within the fine-grained samples (10057, 15556), a minimum segmented particle size of seven voxels was chosen. As XCT does not resolve crystallographic axes, particle orientation for the mineral phases discussed here is related to their external shape (i.e., crystal habit). This derived shape and orientation data was used to determine if any foliation and/or lineation fabric was present within the sample volumes using strain analysis described below.

As it was not possible to create a mask for the external portion of sample 15556 due to computational limitations, a different approach was taken to extract vesicles in this sample. The "outside" was segmented and separated as one component with the vesicles, which had similar greyscale values. Once extracted, the particle volumes in the combined "outside"/vesicles component were evaluated to determine the value at which volumes became massive and represented thousands of voxels touching each other "outside" of the sample, not finite vesicles. The blobs determined to be representative of "outside" were discarded. To evaluate the success of this approach, the more vesiculated samples (10057, 12038, and 70017) were analyzed without a mask and compared to their masked versions. In all cases, the vesicularity of the samples changed by $\sim 1\%$. We are therefore confident that the separation and resulting volumetric analyses of sample 15556 were accurate despite having no mask. All other data from sample 15556 was extracted as described earlier.

2.2.1. *Investigation of extracted clusters*

To evaluate whether including particle clusters without separating them would significantly affect further interpretation, manual separation of oxides in sample 10057 was additionally undertaken. This sample was chosen because 1) it is a high-Ti basalt and thus has one of the highest oxide contents of the samples studied here making it more likely to be affected by clustering, and 2) the 10057 dataset was not as significantly altered by beam hardening as 70017, the other high-Ti sample with similarly high oxide volume (described further below). Using no separation, over 100,000 oxide particles were found to exist in 10057,19. Observing all of them and separating any clusters manually required 2.5 h per 1% of sample volume traversed. Thus, a representative subset in the center of the sample was cropped to specifically investigate clusters instead. The subset was approximately one tenth of the total sample volume, and was first analyzed using no separation, and then again using manual observation at a rate of 1% completed every $\sim$ 20 min. During manual separation, any simple clusters (see Fig. S1) found were separated using the "Pick 3 Points" option where 3 points were selected along a connection between two particles. This generated a plane along which the cluster was split into separate particles. For more information, see Ketcham (2005), and the *Blob3D* user manual. Complex clusters (Fig. S1) were separated when possible, though several ($\sim$ 2 to 3% of all particles) were too complicated for this. From this work, the clustered oxides were observed to account for $<$10% of the data in this high titanium sample. Both datasets were evaluated via *Stereonet* (described in section 2.3 Strain analysis) and size distribution analysis (described in section 2.4 Size distribution analyses), and the results are presented in Fig. S2. It was determined that clustering would not significantly influence later textural analyses, and the time involved in manually assessing particles and clusters was not worth the outcome for this study. As a result, manual separation of either oxide or vesicle clusters was not pursued further. All samples were visually examined in *Blob3D* to ensure that none exhibited more oxide or vesicle clustering than 10057 and to ensure this treatment was appropriate. The only

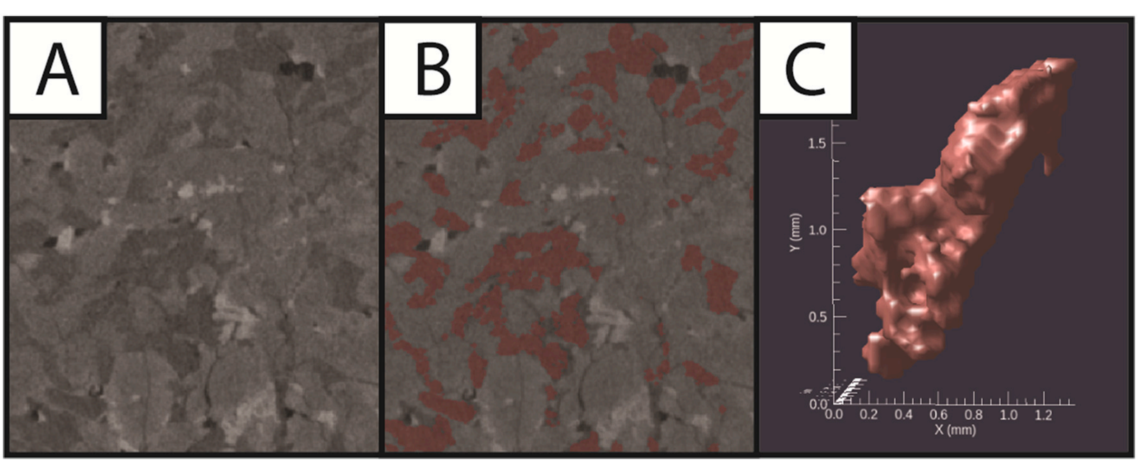

Fig. 2. A summary of the steps involved in extracting particle data from XCT scans. A) An example detail of a scan from sample 15085. B) An unseeded grayscale range has been selected to highlight voxels of a specific component (in this case plagioclase feldspar) in the same field of view as panel A, in order to segment them into components using *Blob3D*. C) A "blob" produced from adjacent voxels, representing a distinct particle. The length, width, depth, volume, and orientation with respect to the sample was extracted from such blobs.

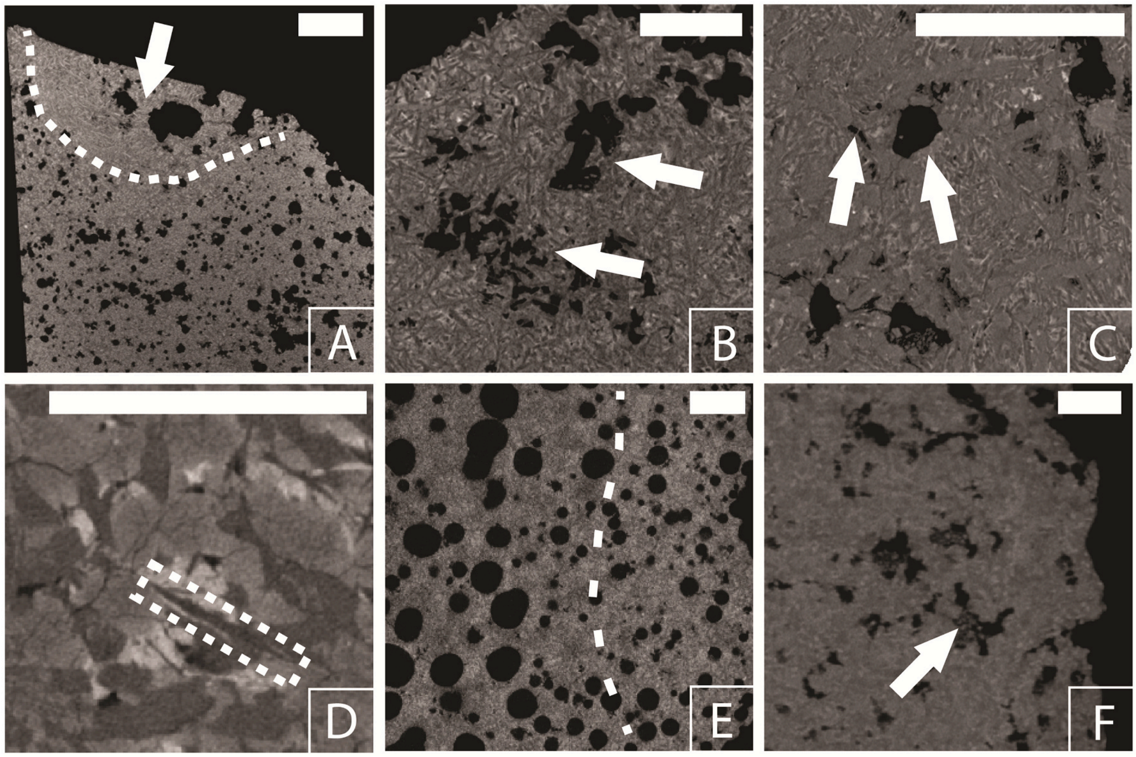

Fig. 3. Regions of interest in each of the samples. Scalebars are 5 mm long in all images. A) Area of sample 10057 showing an entrained enclave, outlined and marked by an arrow. B) Area of sample 12038 showing the gradual transition from vesicles (top right) to a more vuggy population (bottom left), indicated by arrows. C) Area of sample 12043 showing two populations of gas cavities – one made up of rounded vesicles, the other made up of interstitial vugs, indicated by arrows. D) Area of sample 15085 showing the accessory phase tridymite (outlined). E) Area of sample 15556 indicating the approximate gradual transition from a highly vesiculated region to a less vesiculated region. F) Area of sample 70017 showing sample material infilling vesicles, indicated by an arrow.

instance where clustering was more significant was in the case of vesicles in 15556. Out of the 91,503 vesicle blobs extracted in 15556 using the methods described in section 2.2, the largest 260 blobs were clusters. These clusters accounted for ~ 94% of the vesicle volume despite their relatively small frequency. Because clustering here could sway subsequent results, we assessed how removing the 260 blobs would change stereographic (see section 2.3; Fig. 4) and size distribution (see section 2.4; Figs. 5-6) investigations. The results of analyzing data without clusters are presented in Fig. S3. The stereonet without clusters (Fig. S3) is near identical to the stereonet with clusters (Fig. 4). The size distributions, however, do not align – including the 260 clusters indicates vesicle coalescence (Fig. 6; described further in sections 3. Results, and 4. Discussion), while excluding those clusters suggests vesicle collapse (e.g., Shea et al., 2010). During collapse, vesicles lose their round shape and become irregular (e.g., Mongrain et al., 2008), which is inconsistent with the spherical texture of vesicles in 15556. For this reason, all discussion of sample 15556 is based on analyses including the clusters. Thus, datasets collected via “No separation” were investigated in all instances, and clusters of oxides/vesicles were treated as one.

2.3. Strain analysis

Previous work has suggested that the long axes of crystals may be aligned parallel to flow direction (i.e., Castro et al., 2002; Folkes and Russell, 1980; Martin and Nokes, 1988; Shaw, 1969), and vesicles may experience elongation due to strain (Lejeune et al., 1999; Okamura et al., 2009; Passey and Bell, 2007; Shea et al., 2010). The role of strain during flow and the generation of associated petrofabrics is not completely understood, as there are a number of fabrics beyond lineation and foliation that can be potentially preserved (e.g., Nicolas, 1992; Paterson et al., 1998, 2019). However, parallel alignment of crystals as well as elongation of vesicles in the direction of flow is one of the simplest interpretations of a petrofabric and is one of the most straightforward to quantify. In order to interpret any potential strain recorded by a lunar lava upon emplacement, extracted shape preferred orientation data was plotted on rose diagrams and on stereographic projections (contoured using Kamb) via *Stereonet 11* (version 11.3, Allmendinger et al., 2012; Cardozo and Allmendinger, 2013) (where particles were treated as unidirectional vectors). Computational limits while using *Stereonet* led to the 10,000 particles of greatest volume being analyzed. It was assumed here that particles of all sizes would have recorded the same degree of strain, and thus our particle volume limitation should have no effect on orientation distribution interpretations. Sample fabrics were further investigated via the methodology outlined by Woodcock and Naylor (1983). Eigenvectors, and associated eigenvalues, of the particle distribution were calculated via *Stereonet 11* using the Bingham Analysis option. Then, the *K*-value and *C*-value were calculated following the method described by Woodcock and Naylor (1983) using the derived eigenvalues. The *K*-value describes the shape of the distribution:

$$K = (ln(S1/S2))/(ln(S2/S3)) \quad (1)$$

where S1 is the largest eigenvalue, S2 is the intermediate eigenvalue, and S3 is the smallest eigenvalue. If $K > 1$, the distribution can be considered as clustered, and if $K < 1$, the distribution is girdled. The *C*-value, describes the strength of the fabric (i.e., how tightly the data is oriented in the mean vector direction, Woodcock and Naylor, 1983):

$$C = ln(S1/S3) \quad (2)$$

Together, these parameters were used to evaluate the stereographic data distributions and the presence of possible fabrics within the samples.

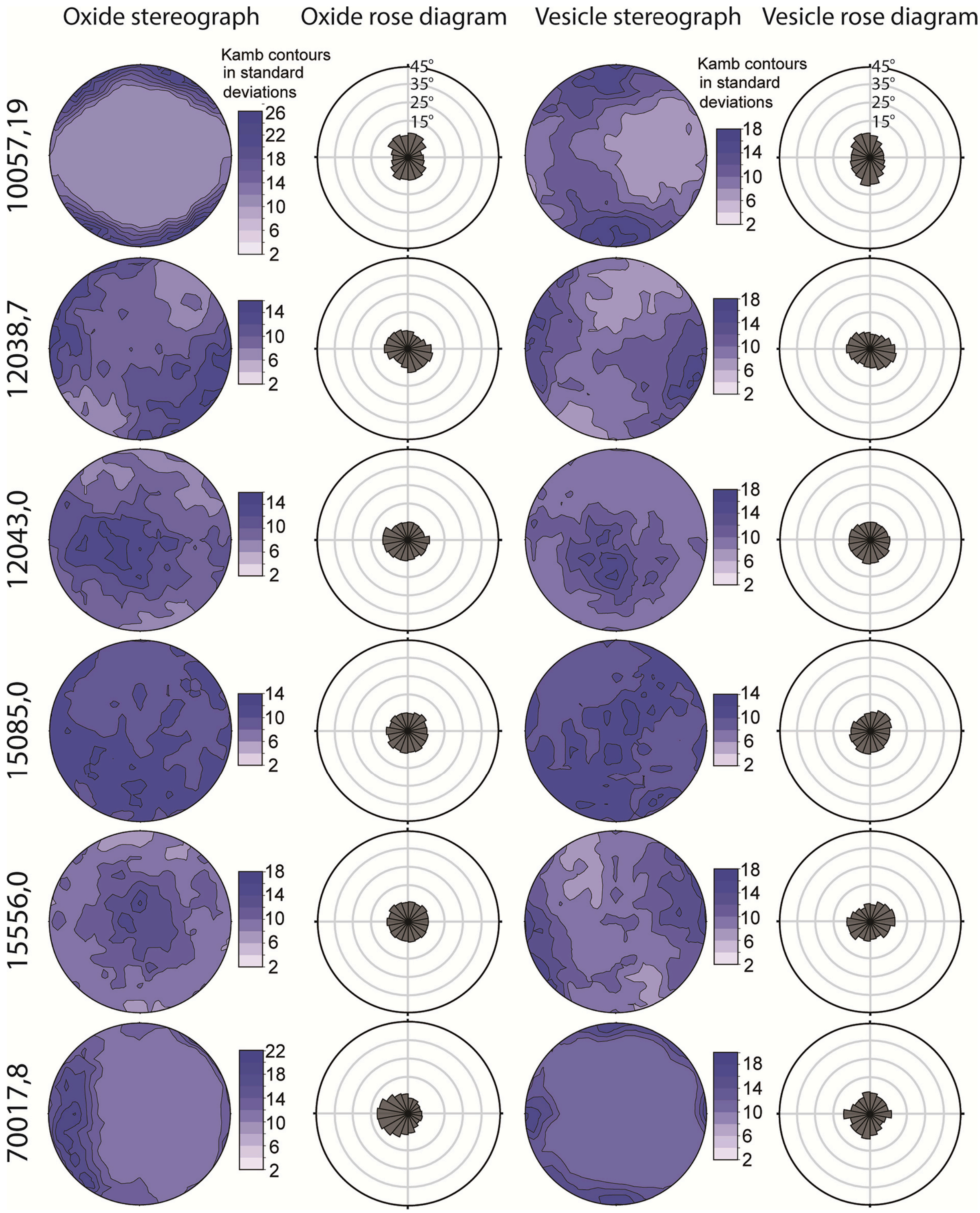

Fig. 4. Stereographic projections and rose diagrams generated via *Stereonet 11* (Allmendinger et al., 2012; Cardozo and Allmendinger, 2013) based on the 10,000 particles of greatest volume. Data plotted here is the longest axis of particles or vesicles/vugs. See also Table S3 for *K*-values and *C*-values. (For interpretation of the references to colour in this figure legend, the reader is referred to the web version of this article.)

2.4. Size distribution analyses

Calculated particle volumes were utilized to examine the particle size distributions (PSDs, e.g., Friedrich et al., 2008; Jerram and Higgins, 2007) of oxides (i.e., ilmenite and spinel). Vesicle size distributions (VSDs, e.g., Shea et al., 2010) were used to examine the vesicle component within each sample. In both cases an X-Y diagram compared the population density (proxy for crystal nucleation rate) with particle/vesicle volumes (proxy for crystal growth rate) in a process similar to crystal size distribution (CSD) analysis (Higgins, 2000; Morgan and Jerram, 2006). Combined, these parameters were used to evaluate the rate of magmatic cooling (e.g., Donohue and Neal, 2015; Morgan and Jerram, 2006; Neal et al., 2015). While CSD analyses rely on estimating a crystal's third dimension (Higgins, 2000), all three dimensions of a

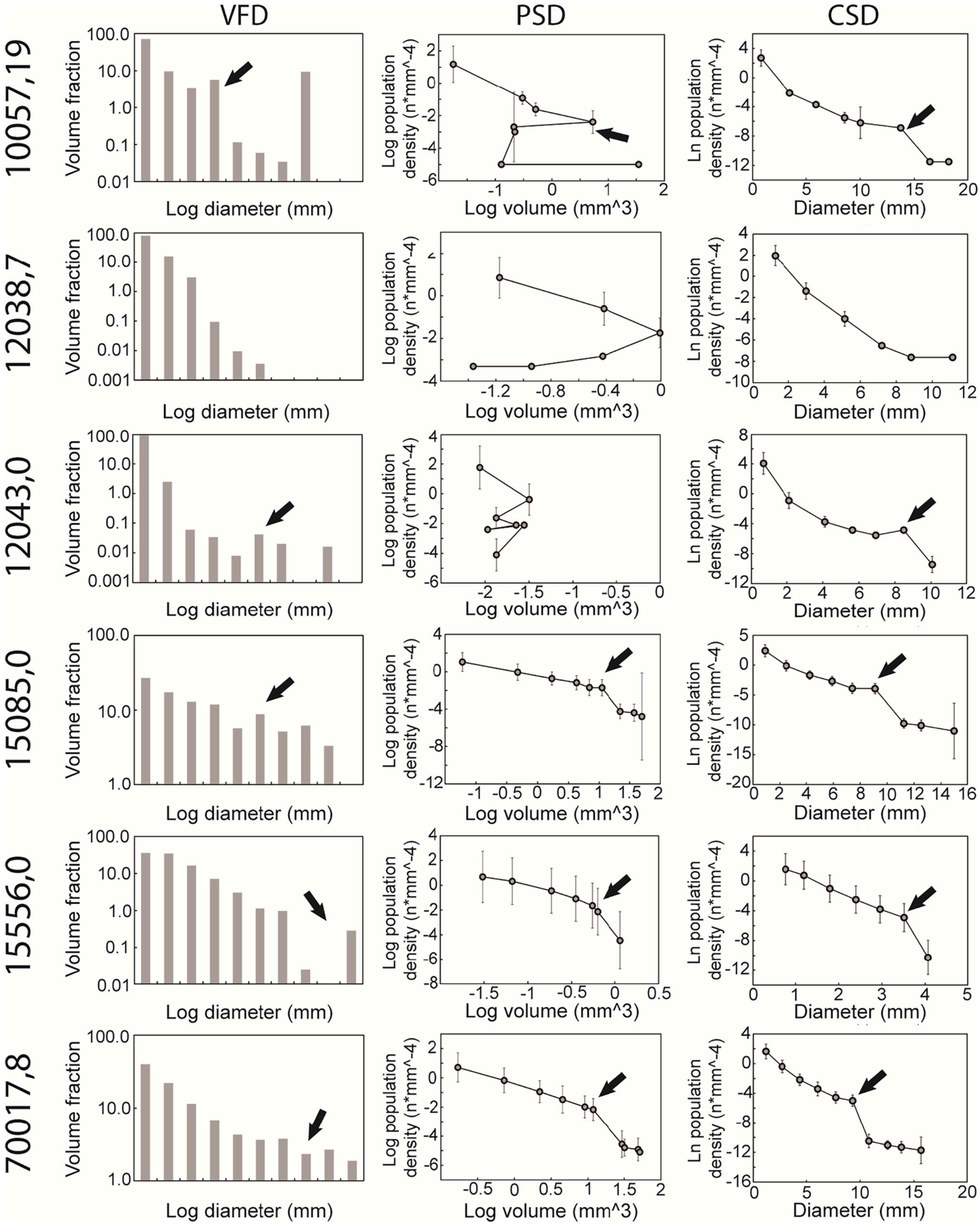

Fig. 5. Volume fraction distributions (VFDs, left), particle size distributions (PSDs, center), and crystal size distributions (CSDs, right) for the oxide phases in studied samples based on the 15,000 particles with the greatest volume. Arrows indicate apparent "kinks" which suggest a change in cooling environment. See text for discussion.

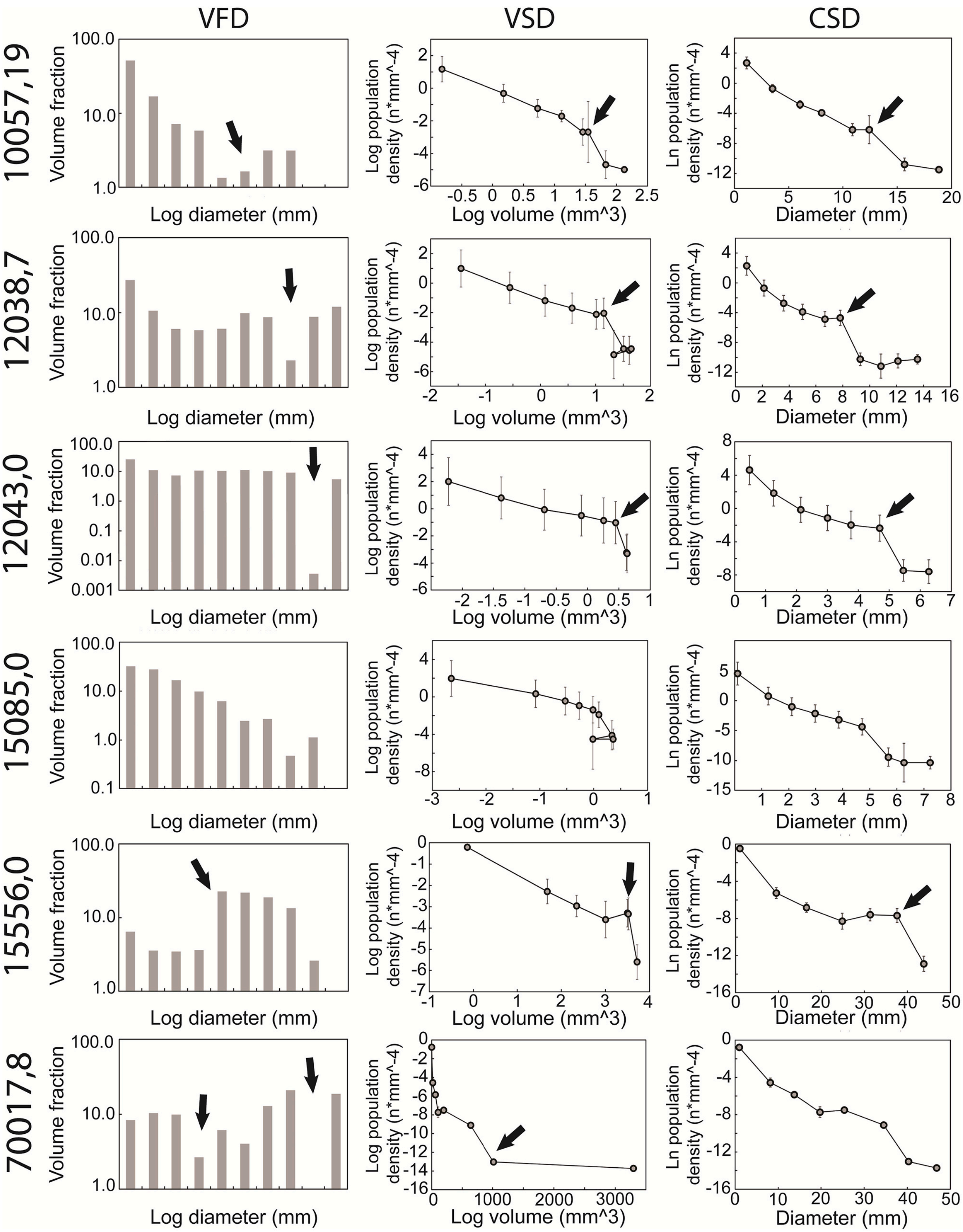

Fig. 6. Volume fraction distributions (VFDs, left), vesicle size distributions (VSDs, center), and crystal size distributions (CSDs, right) for the vesicles and/or vugs in studied samples based on the 15,000 particles with the greatest volume. Arrows indicate apparent "kinks" which suggest a change in cooling environment. See text for discussion.

particle are defined via XCT. The work of Higgins (2000) and Morgan and Jerram (2006) developed standard methods that are now widely used to generate CSDs based on crystal parameters calculated from 2D observations (e.g., in a thin section). Here, an Excel spreadsheet called 3DSD (see supplementary materials) was developed based on the work of Higgins (2000) and Morgan and Jerram (2006) to automatically quantify PSD, CSD, and VSD profiles from 3D XCT data. Data was separated into 10 bins based on particle length. From this, average particle volume, and average particle diameter for each bin was calculated. Volume fraction was also calculated to aid in the visualization of volume fraction size distributions (VFDs). Calculated parameters were then graphed in a series of X-Y diagrams to support evaluation of sample textural characteristics and comparison to CSDs. To support data visualization, log of population density was plotted vs. log of average particle volume. This is different to traditional CSDs. PSDs and VSDs plotted identically to CSDs (ln population density plotted vs. particle volume) can be found in Fig. S4. For simplification purposes, only 15,000 particles or vesicles of greatest volume were evaluated. Interpretation of the shape and size of small particles can be challenging (e.g., Donohue and Neal, 2015), therefore omitting the smallest particle population is unlikely to impact data interpretations.

3. Results

3.1. Mineralogy

The extracted volume-based modal mineralogies of each sample are summarized in Table 1. In summary, all extracted volumetric mineralogies reported here are similar to the ranges of the modal mineralogies reported previously. As expected there was some variation, as different sample splits were studied here and not all phases were individually accounted for (e.g., olivine). Nonetheless, the general similarity in modal abundances reported via 2D and 3D indicated that previously reported sample component proportions were accurate. Thanks to its distinct composition and characteristic crystal habit (e.g., Fig. 3D), it was even possible to segment tridymite data in sample 15085. Vesicle volumes also match previously reported values for samples 10057, 12038, and 15556 (Table S2; Meyer, 2016, and references therein).

Sample 70017 was the largest sample investigated here, and did not initially match modal mineralogies reported by previous authors. For example, the initial oxide volume was 14.5% lower (Meyer, 2016, and references therein). To account for its large size relative to other samples (16.5 cm at its widest, as opposed to the other samples which were $<$ 10 cm wide), 70017 was scanned at 450 keV, while the remaining samples were all scanned at X-ray energies of $<$ 250 keV (Table S1). Higher energy X-rays are necessary to penetrate larger samples, but are less sensitive to changes in sample density and chemistry (Ketcham and Carlson, 2001; Hanna and Ketcham, 2017). This made voxels of different components difficult to distinguish. In addition, the scan of 70017 had a beam hardness artifact due to the sample's large size and density, which prevented the whole sample from being segmented accurately (e.g., Hanna and Ketcham, 2017). To address this, the sample exterior was cropped away, leaving behind $\sim$ 40% of the interior which was analyzed again via *Blob3D*. By studying only the interior of 70017, much of the variation in grayscale values along the sample rim due to beam hardening was eliminated. This facilitated phase separation despite the challenges associated with a scan energy of 450 keV. The volumetric mineralogies from the interior of sample 70017 matched previously reported modal mineralogies much more closely (Table 1). It was this latter analysis of 70017 that was used in the mask vs. no-mask comparison of 15556 and sample vesicularities described in section 2.2. Based on the cropping that was necessary, future studies may want to consider scanning smaller sample pieces in order to avoid XCT scanning artifacts and improve analysis (Hanna and Ketcham, 2017). This would also allow the usage of lower energy X-rays, which would aid in component distinction (e.g., Ketcham and Carlson, 2001).

3.2. Textural observations

Sample 10057 is fine-grained (0.1 to 0.3 mm), and vesicular (11.5%). The vesicles in this sample have an aspect ratio of 1.9 $\pm$ 0.6, indicating that vesicle shapes vary (Fig. 1A-D, Fig. S5). Texturally, there was no indication that crystals of any phase in this sample are oriented, which was consistent with the plotted shape preferred orientations (Fig. 4; described further in section 3.3). The distribution of vesicles in 10057 was observed to be uniform, except for the region shown at the top of the sample in Fig. 1A and detailed in Fig. 3A. This region is less vesiculated and visually coarser-grained than the surrounding finer-grained basalt (Fig. 3A). The transition between these sample regions is abrupt, thus suggesting that this is an entrained enclave (see Fig. 3A for detail). From bulk rock work on sample 10057, Jerde et al. (1992) noted chemical heterogeneity in rare earth elements content; the presence of texturally and mineralogically distinct fragments may, in part, account for this variation.

Sample 12038 is holocrystalline and has an average grain size of $\sim$ 0.6 mm (Meyer, 2016, and references therein). The vesicles/vugs in this sample have highly irregular shapes, resulting in an average aspect ratio of 2.4 $\pm$ 0.8. This sample is dominated by acicular plagioclase feldspar grains which were observed to exhibit subophitic textures and enclose pyroxene grains (Fig. S6). This is consistent with its classification as a feldspathic basalt. Much of this sample was found to contain only irregularly shaped vugs that are bound by mineral grains. A small portion of this sample preserves larger cavities that are distinct in their morphology (Fig. 3B) and dominate the total vesicularity of this sample (which is 3.7%). The transition between these two regions is gradual, with no clear textural change in the mineralogy of the sample (see Fig. 1E-F; see also Fig. 3B and Fig. S6). The region characterized by small vugs can be described as having diktytaxitic texture (e.g., Wilmoth and Walker, 1993). The significance of this textural characterization is described in greater detail later (see section 4, Discussion).

Sample 12043 is a medium-grained ($\sim$ 1 to 3 mm pyroxene grains in a matrix of $\sim$ 0.5 mm grains) pigeonite basalt and is holocrystalline (Fig. 1). On the basis of the data collected here, some pyroxene crystals were found to be macrocrystic with finer-grained interstitial pyroxene, plagioclase, and rare oxides. This sample also contains small vugs that define a diktytaxitic texture (Wilmoth and Walker, 1993), and a few rounded vesicles all of which are uniformly distributed (Figs. 1I-L, 3C, S7). Although this sample is not highly vesiculated (2.7%), it does preserve the highest vesicle aspect ratio of all samples (3.4 $\pm$ 1.9). The vugs and vesicles are not oriented in any particular direction indicating the high aspect ratio is likely due to vug shape variation, and not elongation. This is described further in section 3.3.

Sample 15085 is the coarsest-grained ($\sim$ 5 mm) sample studied here (Fig. 1M-P, and Fig. S8), and has previously been described as microgabbroic (e.g., Grove and Walker, 1977). Large euhedral plagioclase and pyroxene crystals are present with finer-grained pyroxene and plagioclase grains present as interstitial. Plagioclase poikilitically encloses some of the pyroxenes. This sample is also the least vesiculated of all samples studied here (0.6%) with only rare, small vugs dispersed throughout the sample (see Figs. 1 and 3D). The average aspect ratio of these vugs is 2.7 $\pm$ 1.1, but once again this is attributed to irregular vug shapes, not elongation. This is because elongation mechanisms would align vugs in a specific direction, and this was not observed in the stereonet projection (Fig. 4; Passey and Bell, 2007). In addition to being able to distinguish and extract tridymite information, zonation within individual pyroxene grains was revealed (Fig. 3D). Here, zonation is normal (i.e., trending towards Fe-rich rims), which, combined with the coarse-grained nature of this sample, indicated that 15085 experienced a slow cooling environment during crystallization, consistent with the conclusions of Grove and Walker (1977) and Takeda et al. (1975).

Sample 15556 is holocrystalline, fine-grained ($\sim$ 0.4 mm, Meyer, 2016, and references therein), and contains minor porphyritic grains of what appeared to be pyroxene, though olivine macrocrysts have also been noted in this sample (Ryder, 1985). This sample is also highly vesiculated (48.0%), but the vesicles have the lowest aspect ratio of all the samples studied here, at 1.5 ± 0.6. The vesicularity reported here for sample 15556 is consistent with previous studies (Table S2, Meyer, 2016, and references therein), although the mineralogy is not. A portion of this sample contains a region with notably smaller vesicles (Fig. 3E, S9). This area of interest (on the right in Fig. 3E) was cropped and re-analyzed via *Blob3B*. Its vesicularity is ~ 12%.

Because of the large size of sample 70017, the use of higher energy X-rays was necessitated. This decreased relative attenuation and required a lower imaging resolution. The following observations are based on the cropped evaluation of sample 70017 (see section 3.1). This sample is holocrystalline, medium-grained (up to 2 mm), and vesicular (10.1%). The vesicularity of this sample is defined by numerous irregularly shaped vesicles with an average aspect ratio of 2.4 ± 0.8. Some of the largest vesicles were partly filled with chipped sample material (Fig. 3F, S10). This likely contributed to irregularity of vesicle shapes and could account for the higher aspect ratio.

3.3. Strain evaluation

Shape preferred orientations of oxides and vesicles are summarized as stereographic projections and rose diagrams in Fig. 4. Orientation distributions of oxides and vesicles in samples 12038 and 12043 were found to be internally consistent and oriented in cluster distributions (*K*-values >1, see Table S3). In contrast, samples 10057, 15085, 15556, and 70017 were not internally consistent with respect to their oxide and vesicle shape preferred orientations. As summarized by rose diagrams presented in Fig. 4, neither oxides nor vesicles are strongly foliated or lineated, suggesting these samples did not experience strain to a degree that imparted a petrofabric. To evaluate this further, the statistical test described by Woodcock and Naylor (1983) was employed to assess the shape (*K*-value, eq. [1]) and strength (*C*-value, eq. [2]) of each petrofabric. We remind the reader that both parameters are dimensionless units calculated from the eigenvalues of an orientation distribution. From Woodcock and Naylor (1983), a fabric is strong if the *C*-value is near to or greater than 3; a C-value below 3 indicates a weak fabric where particle orientations are close to random. As shown in Table S3, none of the distributions had a *C*-value >1; in fact, most distributions range in *C*-value from 0.1 to 0.4, indicating that these lavas experienced little strain during emplacement and solidification on the lunar surface. However, it is important to recognize here that the two samples with highest clustering visually (10057 and 70017) in Fig. 4 also had the highest *C*-values (0.86 and 0.7, respectively, Table S3) for their oxide distributions. Both samples have K-values of <1 (Table S3) which indicates girdle distributions. Sample 10057 and 70017 may be the only samples studied here that have preserved some small degree of foliation as a result of emplacement.

3.4. Analysis of particle and vesicle size distributions

The size distributions of oxide phases and vesicles are presented in Figs. 5 and 6, respectively, and were interpreted within the context of previously published work (e.g., Higgins, 2000; Morgan and Jerram, 2006). For application specifically to lunar samples, the reader is referred to Donohue and Neal (2015) and Neal et al. (2015). For vesicle distributions, the reader is referred to the work of Shea et al. (2010). The PSDs presented in Fig. 5 summarize "oxides" which could comprise several mineral phases with different crystal habits, such as equant ulvöspinel or chromite, and elongated ilmenite. However, phases such as ulvöspinel and chromite typically comprise a minor component in lunar basalts (generally <0.2%; Meyer, 2016 and references therein), whereas ilmenite is relatively more abundant and forms larger crystals, particularly in the high-titanium basalts (10057 and 70017). As only the 15,000 particles of greatest volume are represented in Fig. 5, it was assumed that phases other than ilmenite would not significantly impact oxide size distributions for any of the samples studied here.

Samples 10057, 12043, 15085, 15556, and 70017 all preserved a "kink" in their oxide PSD (Fig. 5; see also Figs. S1A-B for an example of the two populations in 10057). 12038 is the only sample where size distributions were close to linear. This sample, however, is a low-titanium basalt and did not contain abundant crystals of ilmenite, hence it was challenging to interpret the oxide distribution (2.7 vol. %, see Table 1). Samples 12043, 15085, and 15556 are also low-titanium basalts and contained minor amounts of oxide particles (1.2%, 4.9%, and 1.2%, respectively), therefore the interpretation of a "kink" is likely not attributable to the samples' entire cooling history. In terms of VSDs, samples 10057 and 15085 record a single stage of growth. Samples 12038 and 12043 preserved a "kink" in their VSDs (Fig. 6), indicating the existence of at least two vesicle populations. The vesicles in samples 12043 and 70017 also record some degree of vesicle coalescence. Meanwhile, the vesicle record of sample 15556 (see VFD in Fig. 6) preserves clear evidence of vesicle ripening when compared to the work of Mangan and Cashman (1996) and Shea et al. (2010). During ripening, volatile species diffuse between bubbles, increasing bubble size but decreasing bubble number (Mangan and Cashman, 1996). This process likely accounts for the relatively large vesicle sizes in sample 15556 (Fig. 1Q-T).

At the smallest particle and vesicle sizes, PSDs and VSDs record an upward curved trend in population density. This is opposite to the problem encountered in CSD analyses, where the smallest crystals usually trend downwards in population density due to high uncertainties in their population density calculations (e.g., Cashman, 2020; Castro et al., 2003; Donohue and Neal, 2015). In the PSDs, the upturn is likely the result of a data artifact. The separation methods employed here may have led to the generation of small, false particles from neighboring voxels of similar grayscales, thus inflating the frequency (and resulting population density) of the smallest particles. Alternatively, these trends may exist because of the incorporation of small crystals of minor phases such as chromite and ulvöspinel into the oxide analyses.

4. Discussion

4.1. Lunar lava flow stratigraphy

The characteristics of Apollo samples can be compared to pāhoehoe lava stratigraphy seen on Earth (Donohue and Neal, 2015; Garry et al., 2012; Li et al., 2021b; Roberts and Gregg, 2019; Rumpf et al., 2020; Tolometti et al., 2020; Wilson, 2009). The samples studied here originated from different magmatic systems and represented flows of distinct compositions, but their textures as characterized via XCT were still consistent with physical characteristics seen at different stratigraphic locations within typical terrestrial pāhoehoe flows. In this framework, samples 10057 (11.5% vesicularity) and 15556 (48.0% vesicularity) were interpreted to generally represent the crust of lunar pāhoehoe lava lobes (Fig. 7), consistent with their fine-grained, vesicular textures (Fig. 1A-D, Q-T). More specifically, vesicle size in the lobe crust generally increases towards the center of a lava lobe until the core is reached (Self et al., 1998), so 15556 was interpreted as having formed deeper inside its lobe crust relative to 10057, considering that the vesicles in 15556 are relatively much larger (see Figs. 1, 3, 7). Alternatively, the difference in vesicle shape and size could be related to viscosity differences – this is discussed further in section 4.2. Finally, the zone of relatively low vesicularity identified in sample 15556 (Fig. 3E) may represent the transition between a vesicular zone and a less vesicular zone within a lava lobe (Fig. 7).

Within sample 15556, two regions which are vesiculated to different degrees were observed (48.0% vs. 12.1%, Table S2; see Fig. 3E, and section 3.2). Because lava lobe crusts can consist of alternating bands of more and less vesiculated regions, it was challenging to identify specifically which sample region cooled at a stratigraphically higher location (Fig. 7; e.g., Self et al., 1998; Vye-Brown et al., 2013). On the Moon,

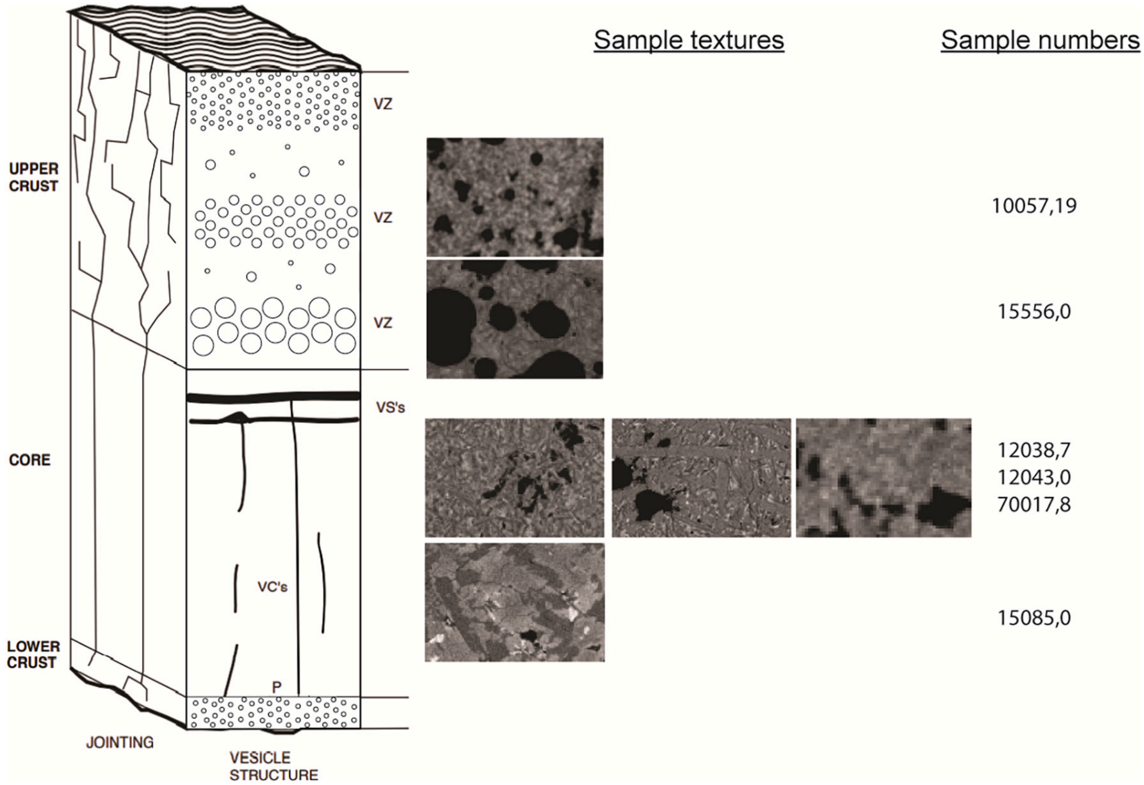

Fig. 7. Idealized schematic indicating the likely stratigraphic location where each sample crystallized within its respective lava lobe based on sample textural properties. All images are 1 cm across. While these samples originated from different magmatic systems and had different compositions and volatile loads, based on their textures samples 10057 and 15556 were interpreted to have cooled in the lobe crust; sample 15085 likely cooled in the lobe core; samples 12038, 12043, and 70017 may mark the transition between these two regions. Modified from Self et al. (1998). Highly vesicular zones in the crust are denoted by "VZ"; Self et al. (1998) additionally noted that vesicle sheets (VS's), vesicle cylinders (VC's), and pipe vesicles (P) can exist in the lobe core, but these were not observed in the samples studied here.

low atmospheric pressures (~ 1 kPa at 1 m depth) would allow gases to rapidly exsolve, and gases near the surface to potentially explode through the crust (Wilson and Head, 2018). Thus, the nature of 15556 precludes it from originating near the top of a flow crust. As observed, the abundance of well-rounded vesicles are consistent with a cooling environment within a relatively thick lava flow (Figs. 1 and 3E; Self et al., 1998), particularly one forming towards the end of an eruption as described by Wilson and Head (2018).

The presence of diktytaxitic textures can record the transition between the crust and core of a pāhoehoe lava lobe (Self et al., 1998; Vye-Brown et al., 2013). The observation of diktytaxitic textures in 12038 (and potentially in 12043) was therefore important within the context of evaluating lunar lava flow lobe stratigraphy, and samples 12038 and 12043 may represent the transition between the lobe crust and core in each of their respective flows. More insulating conditions would exist deeper inside a flow lobe, and would have generated an environment in which bubbles ascend away from the core, consistent with the vesicle size gradation observed in 12038. Specifically, this implies that the larger vesicles could have formed at a higher stratigraphic location than the remainder of the sample (e.g., Self et al., 1998). Additionally, insulating conditions deeper in a lobe would have facilitated crystal growth and prolonged crystallization timescales. This could allow crystals to grow into existing bubbles and generate diktytaxitic textures. It is likely that sample 70017 also formed near the transition between the lobe crust and core. Its medium-grained nature precluded it from having formed in the crust, but its vesicularity (10.1%) indicated that it is unlikely to have formed deep within the lobe core (Self et al., 1998).

Finally, sample 15085 is relatively coarse-grained and less vesiculated (0.6%) relative to the sample suite studied here. Within the context of lava flow architecture, these textural characteristics were consistent with an insulating magmatic cooling environment, such as the core of a lava lobe (Fig. 7). The lack of evidence for exsolved gases in this sample also indicated that any bubbles initially present were removed prior to solidification. For typical terrestrial basalt viscosities, bubbles ascend towards the surface of the lava lobe on the order of days to weeks (Aubele et al., 1988; Manga, 1996; McMillan et al., 1989). This leaves behind a dense lobe core, which is consistent with the textures observed in 15085. Previous work has reported slow, nearly linear cooling rates for sample 15085 (Grove and Walker, 1977). These inferences are consistent with the interpretation presented here that 15085 cooled in a pāhoehoe lobe core. PSD results (Fig. 5) indicated that 15085 experienced a change in its magmatic environment at some point during its crystallization history, such as an eruption event or a chemical change within the magmatic system. This is discussed further in section 4.3. These scenarios may be investigated further and potentially reconciled with detailed in-situ chemical analyses of major silicate phases, but this sample is too coarse-grained to attempt a CSD analysis via thin-section only.

4.2. *Lunar basalt emplacement*

To generate a petrofabric, a small degree of strain is required (Benn, 1994; Paterson et al., 1998). The lower viscosities of lunar magmas would, however, impart less strain during flow and thus would be less likely to align mineral grains (or deform vesicles). There are a couple of scenarios in which vesicles could experience elongation during magmatic ascent or as a result of shear strain (Lejeune et al., 1999; Okamura et al., 2009; Shea et al., 2010). The vesicle populations in the samples studied here did not preserve evidence of either. The lack of significantly strong shape preferred orientations, as indicated by low

C-values, was consistent with the conclusions of previous authors that lunar magmas had much lower viscosities than terrestrial magmas (e.g., Vernon, 2018; Wilson, 2009). The high aspect ratios reported here (see section 3.2) were therefore attributed to shape irregularity, and not to elongation (e.g., Passey and Bell, 2007). The lack of elongation may also be due to overprinting by other processes, such as bubble coalescence (Shea et al., 2010), which was found to be prevalent in at least three of the samples studied here (10057, 12043, and 70017). In the less vesiculated samples, vesicle/vug fabric formation may not have been preserved. This could be due to 1) efficient initial degassing during eruption leading to the removal of volatile species via rapid exsolution, or 2) an initially lower volatile content in the magma (Wilson, 2009; Wilson and Head, 1981, 2018). This is discussed further in section 4.4.

The XCT datasets and accompanying analyses reported here may also provide some additional insight into lunar lava flow thicknesses. For example, the two Apollo 15 samples studied here were consistent with having crystallized within a relatively thick lava flow. Sample 15556 had the largest vesicles of all samples studied here (Figs. 1, 7), consistent with cooling relatively deep inside the crust of a lobe where gases could exsolve and coalesce but could not escape due to the overlying crust (as described in section 4.1; Keszthelyi and Self, 1998; Self et al., 1998; Wilmoth and Walker, 1993; see also Fig. 7). Additionally, the microgabbroic nature of sample 15085 was also consistent with slow, insulated cooling occurring inside a relatively thick lava flow (10 to 30 m, Grove and Walker, 1977; Neal and Taylor, 1992; see also Keszthelyi and Self, 1998; Neal et al., 2015; Passey and Bell, 2007; Self et al., 1998; Takeda et al., 1975). Despite these similarities, reported differences in petrography and chemical composition preclude these two Apollo 15 samples from originating from the same flow (e.g., Meyer, 2016, and references therein; Neal and Taylor, 1992).

The low-titanium basalts of Apollo 12 and 15 have on average ~ 5 wt. % higher bulk SiO_2 content than the high-titanium basalts of the Apollo 11 and 17 sites (e.g., BVSP, 1981; Gawronska and McLeod, 2019; Papike et al., 1976; Papike et al., 1991; Walker et al., 1975). With bulk wt. % SiO_2 content being one of the major controls on basalt viscosity (e.g., Vernon, 2018), the Apollo 12 and 15 basaltic lavas were likely slightly more viscous. More viscous lavas create thicker flows (Rowland and Walker, 1988), which suggests that lava flows near the Apollo 12 and 15 landing sites are potentially thicker than their basaltic counterparts at the Apollo 11 and 17 landing sites.

If this is true, the high TiO_2 and low SiO_2 flows near the Apollo 11 and 17 sites were less viscous and could have been characterized by eruptions with slightly higher effusion rates (BVSP, 1981; Garry et al., 2012; Head and Wilson, 1992; Vernon, 2018). On Earth, basaltic lava flow emplacement that is confined within a lava tube or channel has been demonstrated to lead to increased lava flow rates (Dietterich et al., 2015; Keszthelyi and Self, 1998; Rowland and Walker, 1988, 1990). If high effusion rates for lunar volcanism corresponded locally to rapid emplacement (as has been theorized by Head and Coffin, 1997), this may also induce higher strain (Hon et al., 1994; Keszthelyi and Self, 1998; Passey and Bell, 2007; Rowland and Walker, 1988). Within this context, it could be argued that samples 10057 and 70017, which recorded low, but relatively higher strain as compared to the other samples (Fig. 4, Table S3), could have been emplaced more rapidly, for example within a lava tube (Roberts and Gregg, 2019; Spudis et al., 1988; Swann et al., 1972). It is less likely that these samples formed in a channel such as a lunar rille, as lavas traveling in a rille would have a vesicularity close to 0 (Wilson and Head, 2018).

4.3. Effects of crystal and vesicle cargoes

PSD work presented here indicates that all samples except for 12038 contained two populations of oxides (Fig. 5), indicating that crystals have multiple petrogenetic histories. This may correspond to pre-eruptive and post-eruptive cooling episodes resulting in mineral crystallization and gas exsolution (e.g., Donohue and Neal, 2015; Lejeune et al., 1999). Alternatively, multiple crystal populations could correspond to the identification of texturally distinct regions within these samples (e.g., the enclave incorporated in sample 10057). This is important to note because higher crystal contents have the ability to change the internal properties of a lava (Belousov and Belousova, 2018; Bergantz et al., 2017; Lejeune et al., 1999; Nicolas and Ildefonse, 1996; Paterson et al., 2019; Rumpf et al., 2020; Vernon, 2018), which can result in an increase in viscosity (Keszthelyi and Self, 1998; Lejeune et al., 1999; Nicolas, 1992; Nicolas and Ildefonse, 1996; Paterson et al., 1998, 2019; Shaw, 1969; Whitford-Stark, 1982). Vesicles, meanwhile, can either decrease or increase viscosity (Llewellin and Manga, 2005). Altogether, crystal and vesicle content could change the strain experienced by the lava/magma (Nicolas and Ildefonse, 1996; Paterson et al., 2019). The strain recorded by samples studied here is minimal (Fig. 4), except perhaps for samples 10057 and 70017 (Fig. 4; Table S3). The slightly higher strain recorded by samples 10057 and 70017 could therefore be due to the presence of multiple crystal and vesicle populations (Figs. 5 and 6). Overestimation of large particle sizes due to the lack of grain separation may however impact PSD and VSD interpretations (see section 2.2). Nonetheless, crystal and vesicle populations existing prior to solidification in the 10057 and 70017 lavas may have led to increased viscosities, and thus increased strain imparted on these samples during solidification.

It is possible that petrofabrics within lunar lava flows overprint one another, which has been noted on Earth (e.g., Žák et al., 2007). For example, sample 12038 preserved two vesicle/vug populations, which is consistent with vesicle shapes ranging from rounded clusters to interstitial vugs (Fig. 3B). However, it was difficult to evaluate the process (es) through which the vesicles formed, as their shapes were overprinted by the later growth of crystals and formation of the diktytaxitic textures (Fig. 3B). Meanwhile, sample 12043 records two distinct stages of cooling in both oxide and vesicle size distributions (Figs. 5 and 6), indicating that this sample experienced two distinct stages of crystal and vesicle growth. The macrocrystic pyroxene crystal population of 12043 existing alongside a population of finer-grained pyroxenes (see Figs. 1 and 3C) likely also corresponds to a change in cooling environment. No significant degree of strain is recorded by this sample, indicating that any potential crystal effects associated with strain were either nonexistent, insignificant, overprinted, or too complicated to distinguish here. In samples 10057, 15085, 15556, and 70017 the mean planes of oxide and vesicle orientation distributions were not consistent. This may indicate that multiple strain-related mechanisms were involved. For example, strain from buoyancy may have imparted a greater effect on rising bubbles than strain from flow. In this scenario, the original flow fabric would be overprinted (e.g., Aubele et al., 1988; Polacci and Papale, 1997). Alternatively, the samples may have only experienced a minimal amount of strain. The extent to which different components of strain contribute to petrofabrics in lunar basalts, as well as the extent to which petrofabrics are preserved within the Apollo basalt sample suite should therefore be examined further in order to investigate these potential scenarios. Additional Apollo basalt sample characterization must be completed via experimental and analog studies in order to evaluate these emplacement dynamics, particularly for each landing site location. Future in-situ sampling of basaltic lava flows on the lunar surface should be informed by knowledge of flow architecture and an understanding of lobe geometry. This would support the collection of sample suites which fully represent the characteristics and spatial extent of lunar lava flows.

4.4. Effects of volatiles on lunar eruptions

Within the framework proposed by Wilson and Head (2018), samples 12038 and 12043 may have formed during stage 3 of eruption when vesicularity is low but increasing, while samples 10057 and 70017 may have formed later during their respective eruption events, preserving their volatile content. However, flow rates are minimized during the later stages of the Wilson and Head (2018) model which is not consistent with the low, but relatively higher, strain imparted upon 10057 and 70017 when compared to the other samples, unless they formed in a lava tube as described in section 4.2. Alternatively, 10057 and 70017 may have formed earlier from lavas which were initially volatile-rich. Sample 15085, may have formed during the intermediate stage 2 of the eruption where a high flux of Hawaiian-style effusive flow dominated and vesicularity was near 0 (Wilson and Head, 2018). At this stage, lava lakes are generated and could facilitate the formation of coarse-grained textures at stratigraphically low locations (see Fig. 7; McCarter et al., 2006). It is not currently possible to measure lava flow thicknesses and properties directly in the field on the Moon, and distinguishing individual lava flows through remote sensing alone proves to be challenging (e.g., Rumpf et al., 2020). From Wilson and Head (2018), lavas with the highest vesicularity are associated with the final stages of eruption and are characterized by Strombolian-style vesicular flow. At this stage, flows that are injected into previous lobes maintain their vesicularity while erupted flows become foams. Sample 15556 cannot be a foam as it contains less than the 60% to 70% vesicles required of foams (Mangan and Cashman, 1996). Instead, the lava which formed 15556 likely intruded into an inflating lobe. This scenario is consistent with the stratigraphic interpretation presented in Fig. 7.

The VSD analyses performed here could shed further light on the role of volatiles during lunar lava emplacement. Mangan and Cashman (1996) argue that vesicle ripening is a late-stage effect that post-dates initial volatile exsolution, so the vesicle ripening observed in 15556 could also indicate that this sample was not quenched during eruption on the surface and instead cooled in an environment where ripening was possible. Furthermore, bubble migration due to relatively low lava viscosity could explain the lack of volatile species that is preserved in coarse-grained sample 15085. Alternatively, 15085 was produced by a magma with initially low volatile contents, in contrast to the highly vesiculated nature of 15556. Sample 15085 is a quartz-normative basalt, and 15556 is an olivine-normative basalt, hence they likely originated from distinct sources within the lunar mantle (Neal and Taylor, 1992; Rhodes and Hubbard, 1973). As the lunar mantle is likely heterogeneous with respect to volatile contents (McCubbin et al., 2015), the potentially distinct source regions of 15085 and 15556 could explain the variations in vesicle content of the Apollo 15 lavas. Meanwhile, samples 10057, 12043, and 70017 were found to record evidence of vesicle coalescence (Fig. 6; see also Shea et al., 2010). This is consistent with the low viscosities of lunar magmas which would have facilitated bubble migration and coalescence relatively easily compared to higher viscosity magmas (Manga, 1996; Manga and Stone, 1995).

Vesicle volume also has implications for evaluating the volatile load of lunar magmas (e.g., Wilson and Head, 2018). The Moon is generally depleted in volatile species relative to other rocky bodies (e.g., see summaries by McCubbin et al., 2015, and Day and Moynier, 2014). However, volatile species including S, CO, CO_2, H_2O, H_2, F, and Cl have been observed (e.g., Hauri et al., 2015; Wetzel et al., 2015) and modeled (e.g., Newcombe et al., 2019: Nicholis and Rutherford, 2009) to exist on the Moon. Specifically, CO had long been proposed as the primary volatile species responsible for the generation of pyroclastic deposits and vesicular basalts on the Moon (e.g., Fogel and Rutherford, 1995; Nicholis and Rutherford, 2009; Sato, 1979; Wetzel et al., 2015). This necessitates the existence of graphite within the lunar mantle (e.g., Nicholis and Rutherford, 2009), which has only been found in one sample (impact melt breccia 72255).

In 2008, Saal et al. showed that the cores of low-Ti lunar volcanic glass beads contain up to 46 ppm H_2O, 40 ppm, F, and 576 ppm S, with cores of high-Ti beads containing up to 15 ppm H_2O, 15 ppm F, and $\sim$ 400 ppm S, and the cores of very-low-Ti volcanic glasses containing up to 30 ppm H_2O, 10 ppm F, and 270 ppm S (Saal et al., 2008). Researchers have since argued that the sources of these volatile species in the lunar mantle include residual liquid that remained trapped between lunar mantle cumulates after the solidification of the mantle, and nominally anhydrous minerals that contain trace amounts of volatiles (e.g., Liu et al., 2012; Hui et al., 2013; Mills et al., 2014; McCubbin et al., 2015; Potts et al., 2021). The urKREEP reservoir which formed towards the end of the crystallization of the Lunar Magma Ocean and which is enriched in K, rare earth elements, and P, likely also played a significant role in provide volatile species to lunar magmas. McCubbin et al. (2015) proposed that the primary source of volatiles in lunar magmas is the residual urKREEP reservoir and not the lunar mantle. urKREEP could have contributed to the formation of the vesicular samples studied here. Sample 10057 is a member of the high-K Apollo 11 basalt suite, which is proposed to have formed as a result of mantle-derived magma mixing with a KREEPy assimilant (Jerde et al., 1994, and references therein). The incorporation of KREEP-derived volatiles during the petrogenesis of 10057 is thus a possibility and supported by bulk major element chemistry. Several KREEP basalts were collected during the Apollo 15 mission alongside the highly vesiculated 15556 (Ryder, 1985). This sample, however, does not have a KREEPy geochemical signature and thus it is unlikely that its volatile component is derived from KREEP. Given the lack of graphite observed throughout the lunar mare basalt suite, and the recent findings of elevated H abundance in lunar magmas (e.g., Barnes et al., 2013; Greenwood et al., 2011; McCubbin et al., 2010; Tartèse et al., 2013, 2014), we postulate that the more likely volatile species to have produced the vesicles in 15556 and other basalts studied here is H_2.

5. Conclusions

The application of XCT offers planetary geoscientists unparalleled insights into the interior features of extraterrestrial materials. Through the application of XCT to a suite of six basalts from the Apollo 11, 12, 15, and 17 missions it was found that lunar lavas are texturally consistent with terrestrial pāhoehoe lava stratigraphy, indicating that they formed as low-viscosity, effusive flows. This is also consistent with the lack of preservation of any strain-induced petrofabric as demonstrated by the oxide or vesicle populations. PSDs further indicated that basaltic lunar lavas likely contained crystal loads prior to eruption and emplacement on the lunar surface, while VSDs serve as evidence of processes that worked to overprint initial vesicle textures. Specifically, vesicles in several samples record coalescence and ripening. Connectivity modeling of voids within the samples (e.g., Blunt et al., 2013; Moitra and Houghton, 2021; Sok et al., 2009) could shed more light on the textural properties of these vesicles, and the general behavior of bubbles in lunar magmas. Additional work to characterize the role of lunar volatiles would undoubtedly shed more light on the conditions of lava eruption and flow emplacement mechanisms, as well as the stratigraphic correlations of vesicular samples collected during each Apollo mission. As summarized here, XCT can support remote sensing investigations of lava flows on other planetary bodies by providing general constraints on lava properties.

Within the context of sample preservation and curation, XCT significantly improves documentation practices by curating accurate and precise sample reconstructions (Blumenfeld et al., 2017, 2019; Jerram and Higgins, 2007; McCubbin et al., 2019). By acquiring a 3D scan of a sample, XCT data may better inform researchers on sample heterogeneity (e.g., due to brecciation, Zolensky et al., 2014), as is exemplified by the magmatic enclave found here in sample 10057. XCT datasets can also direct researchers to the most advantageous and representative angle at which a sample should be cut into thin section(s) (e.g., Hanna et al., 2015; Jerram and Higgins, 2007). In short, XCT is a powerful analytical and preservatory technique that continues to prove itself as a critical asset to extraterrestrial sample curation and the planetary science community.

Supplementary data to this article can be found online in a Mendeley Data repository (https://data.mendeley.com/datasets/zmkvm7yj94/1).

Declaration of Competing Interest

None.

Data availability

Data for one sample is provided in a linked Mendeley Data Repository; authors do not have permission to share the remainder of data which is owned by the Astromaterials3D project.

Acknowledgements

The authors would like to acknowledge the Apollo astronauts for collecting the lunar samples studied here and all those involved in the Apollo program who made this possible. Sincere thanks are extended to Dr. M. Elise Rumpf and Dr. Jessica Barnes for providing detailed, constructive feedback on this manuscript, as well as Dr. Clive Neal and an anonymous reviewer for their comments on an earlier version of this work. Finally, we acknowledge Dr. Vincent Fernandez for communications regarding parameters used to scan sample 10057 at the National History Museum in London, UK. This research included XCT image data produced by Astromaterials 3D for NASA's Acquisition & Curation Office, funded by NASA Planetary Data Archiving, Restoration, and Tools Program, Proposal No.: 15-PDART15_2-0041.

References

Allmendinger, R.W., Cardozo, N., Fisher, D., 2012. Structural Geology Algorithms: Vectors and Tensors in Structural Geology. Cambridge University Press, New York.

Arif, M., Mahmoud, M., Zhang, Y., Iglauer, S., 2021. X-ray tomography imaging of shale microstructures: a review in the context of multiscale correlative imaging. Int. J. Coal Geol. 233, 103641 https://doi.org/10.1016/j.coal.2020.103641.

Aubele, J.C., Crumpler, L.S., Elston, W.E., 1988. Vesicle zonation and vertical structure of basalt flows. J. Volcanol. Geotherm. Res. 35, 349–374.

Barnes, J.J., Franci, I.A., Anand, M., Tartèse, R., Starkey, N.A., Koike, M., Sano, Y., Russell, S.S., 2013. Accurate and precise measurements of the D/H ratio and hydroxyl content in lunar apatites using NanoSIMS. Chem. Geol. 337-338, 48–55. https://doi.org/10.1016/j.chemgeo.2012.11.015.

Basaltic Volcanism Study Project (BVSP), 1981. Basaltic Volcanism on the Terrestrial Planets. Pergamon Press, Inc, New York.

Belousov, A., Belousova, M., 2018. Dynamics and viscosity of 'a'a and pahoehoe lava flows of the 2012-2013 eruption of Tolbachik volcano, Kamchatka (Russia). Bull. Volcanol. 80 (6) https://doi.org/10.1007/s00445-017-1180-2.

Benn, K., 1994. Overprinting of magnetic fabrics in granites by small strains: numerical modelling. Tectonophysics 233 (3–4), 153–162. https://doi.org/10.1016/0040-1951(94)90238-0.

Bergantz, G.W., Schleicher, J.M., Burgisser, A., 2017. On the kinematics of crystal-rich systems. J. Geophys. Res. Solid Earth 122, 6131–6159. https://doi.org/10.1002/2017JB014218.

Blumenfeld, E.H., Evans, C.A., Oshel, E.R., Liddle, D.A., Beaulieu, K.R., Zeigler, R.A., Righter, K., Hanna, R.D., Ketcham, R.A., 2017. Research-Grade 3D Virtual Astromaterials Samples: Novel Visualization of NASA's Apollo Lunar Samples and Antarctic Meteorite Samples to benefit Curation, Research, and Education. Houston, Texas, Lunar and Planetary Institute, Lunar and Planetary Science Conference XLVIII, Abstract #2874.

Blumenfeld, E.H., Beaulieu, K.R., Thomas, A.B., Evans, C.A., Zeigler, R.A., Oshel, E.R., Liddle, D.A., Righter, K., Hanna, R.D., Ketcham, R.A., 2019. 3D Virtual Astromaterials Samples Collection of NASA's Apollo Lunar and Antarctic Meteorite Samples to be an Online Database to Serve Researchers and the Public. Houston, Texas, Lunar and Planetary Institute, Lunar and Planetary Science Conference XLVIII, Abstract #3056.

Blunt, M.J., Bijeljic, B., Dong, H., Gharbi, O., Iglauer, S., Mostaghimi, P., Paluszny, A., Pentland, C., 2013. Pore-scale imaging and modelling. Adv. Water Resour. 51, 197–216. https://doi.org/10.1016/j.advwatres.2012.03.003.

Brum, J.T., McLeod, C.L., Shaulis, B., Duley, M., Locke, M., 2020. Investigating the History of Allan Hills (ALHA) 81005: What a Meteorite's Components Can Tell Us About its Past. Houston, Texas, Lunar and Planetary Institute, Lunar and Planetary Science Conference LII, Abstract #2919.

Cardozo, N., Allmendinger, R.W., 2013. Spherical projections with OSXStereonet. Comput. Geosci. 51, 193–205. https://doi.org/10.1016/j.cageo.2012.07.021.

Carvalho, L.E., Fauth, G., Baecker Fauth, S., Krahl, G., Moreira, A.C., Fernandes, C.P., von Wangenheim, A., 2020. Automated microfossil identification and segmentation using a deep learning approach. Mar. Micropaleontol. 158, 101890 https://doi.org/10.1016/j.marmicro.2020.101890.

Cashman, K.V., 2020. Crystal size distribution (CSD) analysis of volcanic samples: advances and challenges. Front. Earth Sci. 10 https://doi.org/10.3389/feart.2020.00291.

Cashman, K.V., Kauahikaua, J.P., 1997. Re-evaluation of vesicle distributions in basaltic lava flows. Geology 25, 419–422.

Castro, J., Manga, M., Cashman, K., 2002. Dynamics of obsidian flows inferred from microstructures: insights from microlite preferred orientations. Earth Planet. Sci. Lett. 199, 211–226.

Castro, J.M., Cashman, K.V., Manga, M., 2003. A technique for measuring 3D crystal-size distributions of prismatic microlites in obsidian. Am. Mineral. 88, 1230–1240. https://doi.org/10.2138/am-2003-8-906.

Cnudde, V., Boone, M.N., 2013. High-resolution X-ray computed tomography in geosciences: a review of the current technology and applications. Earth Sci. Rev. 123, 1–17. https://doi.org/10.1016/j.earscirev.2013.04.003.

Cone, K.A., Palin, R.M., Singha, K., 2020. Unsupervised machine learning with petrological database ApolloBasaltDB reveals complexity in lunar basalt major element oxide and mineral distribution patterns. Icarus 346, 113787. https://doi.org/10.1016/j.icarus.2020.113787.

Cunningham, J.A., Rahman, I.A., Lautenschlager, S., Rayfield, E.J., Donoghue, P.C.J., 2014. A virtual world of paleontology. Trends Ecol. Evol. 29 (6), 347–357. https://doi.org/10.1016/j.tree.2014.04.004.

Day, J.M.D., Moynier, F., 2014. Evaporative fractionation of volatile stable isotopes and their bearing on the origin of the moon. Philos. Trans. Royal Soc. Ser. A Math. Phys. Eng. Sci. 372, 20130259. https://doi.org/10.1098/rsta.2013.0259.

Dietterich, H.R., Cashman, K.V., Rust, A.C., Lev, E., 2015. Diverting lava flows in the lab. Nat. Geosci. 8, 494–496. https://doi.org/10.1038/ngeo2470.

Donohue, P.H., Neal, C.R., 2015. Quantitative textural analysis of ilmenite in Apollo 17 high-titanium mare basalts. Geochim. Cosmochim. Acta 149, 115–130. https://doi.org/10.1016/j.gca.2014.11.002.

du Plessis, A., Boshoff, W.P., 2019. A review of X-ray computed tomography of concrete and asphalt construction materials. Constr. Build. Mater. 199, 637–651. https://doi.org/10.1016/j.conbuildmat.2018.12.049.

Ebel, D.S., Rivers, M.L., 2007. Meteorite 3-D synchrotron microtomography: methods and applications. Meteorit. Planet. Sci. 42 (9), 1627–1646. https://doi.org/10.1111/j.1945-5100.2007.tb00595.x.

Fogel, R.A., Rutherford, M.J., 1995. Magmatic volatiles in primitive lunar glasses: I. FTIR and EPMA analyses of Apollo 15 green and yellow glasses and revision of the volatile-assisted fire-fountain theory. Geochim. Cosmochim. Acta 59, 201–215.

Folkes, M.J., Russell, D.A.M., 1980. Orientation effects during the flow of short-fibre reinforced thermoplastics. Polymer 21, 1252–1258.

Friedrich, J.M., Macke, R.J., Wignarajah, D.P., Rivers, M.L., Britt, D.T., Evel, D.S., 2008. Pore size distribution in an uncompacted equilibrated ordinary chondrite. Planet. Space Sci. 56 (7), 895–900. https://doi.org/10.1016/j.pss.2008.02.002.

Gan, M., Zhang, L., Miao, X., Oladyshkin, S., Cheng, X., Wang, Y., Shu, Y., Su, X., Li, X., 2020. Application of computed tomography (CT) in geologic CO_2 utilization and storage research: a critical review. J. Nat. Gas Sci. Eng. 83, 103591 https://doi.org/10.1016/j.jngse.2020.103591.

Garry, W.B., Robinson, M.S., Zimbelman, J.R., Bleacher, J.E., Hawke, B.R., Crumpler, L. S., Braden, S.E., Sato, H., 2012. The origin of Ina: evidence for inflated lava flows on the moon. J. Geophys. Res. 117, E00H31. https://doi.org/10.1029/2011JE003981.

Gawronska, A.G., McLeod, C.L., 2019. Basalts: Insights into Planetary Magmatic Processes from the Moon and Earth. Houston, Texas, Lunar and Planetary Institute, Lunar and Planetary Science Conference X, Abstract #3271.

Gillis, J.J., Jolliff, B.L., Elphic, R.C., 2003. A revised algorithm for calculating TiO2 from Clementine UVVIS data: a synthesis of rock, soil, and remotely sensed TiO2 concentrations. J. Geophys. Res. 108 (E2), 1–18. https://doi.org/10.1029/2001JE001515.

Gillis, J.J., Jolliff, B.L., Korotev, R.L., 2004. Lunar surface geochemistry: global concentrations of Th, K., and FeO as derived from lunar prospector and Clementine data. Geochim. Cosmochim. Acta 68 (18), 3791–3805. https://doi.org/10.1016/j.gca.2004.03.024.

Greenwood, J.P., Itoh, S., Sakamoto, N., Warren, P., Taylor, L., Yurimoto, H., 2011. Hydrogen isotope rations in lunar rocks indicate delivery of cometary water to the moon. Nat. Geosci. 4, 79–82. https://doi.org/10.1038/ngeo1050.

Gregg, T., 2017. Patterns and processes: subaerial lava flow morphologies: a review. J. Volcanol. Geotherm. Res. 342, 3–12. https://doi.org/10.1016/j.jvolgeores.2017.04.022.

Gross, J., Treiman, A.H., 2011. Unique spinel-rich lithology in lunar meteorite ALHA 81005: origin and possible connection to M^3 observations of the farside highlands. Journal of. Geophys. Res. Lett. 116 (E10) https://doi.org/10.1029/2011JE003858.

Grove, T.L., Walker, D., 1977. Cooling histories of Apollo 15 quartz-normative basalts. In: Proceedings of the 8th Lunar Science Conference, pp. 1501–1520.

Hamilton, C.W., 2019. "Fill and spill" lava flow emplacement: implications for understanding planetary flood basalt eruptions. In: NASA Technical Memorandum 220139, pp. 47–56.

Hanna, R.D., Ketcham, R.A., 2017. X-Ray computed tomography of planetary materials: a primer and review of recent studies. Chem. Erde 77, 547–572. https://doi.org/10.1016/j.chemer.2017.01.006.

Hanna, R.D., Ketcham, R.A., Zolensky, M., Behr, W., 2015. Impact-induced brittle deformation, porosity loss, and aqueous alteration in the Murchison CM chondrite. Geochim. Cosmochim. Acta 171, 256–282. https://doi.org/10.1016/j.gca.2015.09.005.

Harris, A.J.L., Allen, J.S., 2008. One-, two- and three-phase viscosity treatments for basaltic lava flows. J. Geophys. Res. 113, B09212. https://doi.org/10.1029/2007JB005035.

Hauri, E.H., Saal, A.E., Rutherford, M.J., Van Orman, J.A., 2015. Water in the Moon's interior: truth and consequences. Earth Planet. Sci. Lett. 409, 252–264. https://doi.org/10.1016/j.epsl.2014.10.053.

Head, J.W., Coffin, M.F., 1997. Large Igneous Provinces: A Planetary Perspective. Large Igneous Provinces: Continental, Oceanic, and Planetary Flood Volcanism.. In: Mahoney, J.J., Coffin, M.F. (Eds.), 100 American Geophysical Union, pp. 411–438.

Head, J.W., Wilson, L., 1992. Lunar mare volcanism: stratigraphy, eruption conditions, and the evolution of secondary crusts. Geochim. Cosmochim. Acta 56, 2155–2175.

Heiken, G.H., Vaniman, D.T., French, B.M., 1991. The Lunar Sourcebook: A User's Guide to the Moon. Cambridge University Press, 736 p.

Hezel, D.C., Friedrich, J.M., Uesugi, M., 2013. Looking inside: 3D structures of meteorites. Geochim. Cosmochim. Acta 116, 1–4. https://doi.org/10.1016/j.gca.2013.01.012.

Hiesinger, H., Head III, J.W., Wolf, U., Jaumann, R., Neukum, G., 2002. Lunar mare basalt flow units: thickness determined from crater size-frequency distributions. Geophys. Res. Lett. 29, 1248. https://doi.org/10.1029/2002GL014847.

Higgins, M.D., 2000. Measurement of crystal size distributions. Am. Mineral. 85, 1105–1116. https://doi.org/10.2138/am-2000-8-901.

Hon, K., Kauahikaua, J., Denlinger, R., MacKay, K., 1994. Emplacement and inflation of pahoehoe sheet flows: observations and measurements of active lava flows on Kilauea Volcano, Hawaii. Geol. Soc. Am. Bull. 106, 351–370.

Howard, K.A., Head III, J.W., 1972. Regional geology of Hadley Rille. In: Apollo 15: Preliminary Science Report. NASA SP-289, pp. 53–58.

Howard, K.A., Head, J.W., Swann, G.A., 1972. Geology of Hadley Rille. In: Proceedings of the 3rd Lunar Science Conference, pp. 1–14.

Hui, H.J., Peslier, A.H., Zhang, Y.X., Neal, C.R., 2013. Water in lunar anorthosites and evidence for a wet early moon. Nat. Geosci. 6, 177–180. https://doi.org/10.1038/ngeo1735.

Jerde, E.A., Snyder, G.A., Taylor, L.A., Liu, Y.G., Schmitt, R.A., 1992. Chemical Composition of Apollo 11 Mare Basalt Rocks: Evidence of Sample Heterogeneity in 10057. Abstracts of the Lunar and Planetary Science Conference, 23, p. 613.

Jerde, E.A., Snyder, G.A., Taylor, L.A., Liu, Y.-G., Schmitt, R.A., 1994. The origin and evolution of lunar high-Ti basalts: periodic melting of a single source at Mare Tranquilitatis. Geochim. Cosmochim. Acta 58 (1), 515–527. https://doi.org/10.1016/0016-7037(94)90480-4.

Jerram, D.A., Higgins, M.D., 2007. 3D analysis of rock textures: quantifying igneous microstructures. Elements 3 (4), 239–245. https://doi.org/10.2113/gselements.3.4.239.

Keszthelyi, L., Self, S., 1998. Some physical requirements for the emplacement of long basaltic lava flows. J. Geophys. Res. 103(11), 27,447–27,464.

Ketcham, R.A., 2005. Computational methods for quantitative analysis of three-dimensional features in geological specimens. Geosphere 1 (1), 32–41. https://doi.org/10.1130/GES00001.1.

Ketcham, R.A., Carlson, W.D., 2001. Acquisition, optimization and interpretation of X-ray computed tomographic imagery: applications to the geosciences. Comput. Geosci. 27 (1), 381–400. https://doi.org/10.1016/S0098-3004(00)00116-3.

Kramer, F.E., Twedell, D.B., Walkton Jr., W.J.A., 1977. Apollo-11 Lunar Sample Information Catalogue (Revised). National Aeronautics and Space Administration Johnson Space Center Contribution #12522.

Lejeune, A.M., Bottinga, Y., Trull, T.W., Richet, P., 1999. Rheology of bubble-bearing magmas. Earth Planet. Sci. Lett. 166, 71–84.

Lemelin, M., Lucey, P.G., Miljković, K., Gaddis, L.R., Hare, T., Ohtake, M., 2019. The compositions of the lunar crust and upper mantle: spectral analysis of the inner rings of lunar impact basins. Planet. Space Sci. 165, 230–243. https://doi.org/10.1016/j.pss.2018.10.003.

Li, C., Hu, H., Yang, M.-F., Pei, Z.-Y., Zhou, Q., Ren, X., Liu, B.L., Zeng, X., Zhang, G., Zhang, H., Liu, J., Wang, Q., Deng, X., Xiao, C., Yao, Y., Xue, D., Zuo, W., Su, Y., Wen, W., Ouyang, Z., 2021a. Characteristics of the lunar samples returned by Chang'E-5 mission. Natl. Sci. Rev. https://doi.org/10.1093/nsr/nwab188 nwab188.

Li, S., Taylor, G.J., Lentz, R., Needham, D.H., Gaddis, L., Shea, T., 2021b. Water Anomalies at Rugged Lava Flows on the Moon. Houston, Texas, Lunar and Planetary Institute, Lunar and Planetary Science Conference XII, Abstract #2508.

Liu, Y., Mosenfelder, J.L., Guan, Y., Rossman, G.R., Eiler, J.M., Taylor, L.A., 2012. SIMS analysis of water abundances in nominally anhydrous minerals in lunar basalts. In: Proceedings of the 43rd Lunar and Planetary Science Conference, Woodlands, Texas, 1866.

Llewellin, E.W., Manga, M., 2005. Bubble suspension rheology and implications for conduit flow. J. Volcanol. Geotherm. Res. 143 (1–3), 205–217. https://doi.org/10.1016/j.jvolgeores.2004.09.018.

Manga, M., 1996. Waves of bubbles in basaltic magmas and lavas. J. Geophys. Res. 101, 17457–17465.

Manga, M., Stone, H.A., 1995. Collective hydrodynamics of deformable drops and bubbles in dilute low Reynolds number suspensions. J. Fluid Mech. 300, 231–263.

Mangan, M.T., Cashman, K.V., 1996. The structure of basaltic scoria and reticulite and inferences for vesiculation, foam formation, and fragmentation in lava fountains. J. Volcanol. Geotherm. Res. 73, 1–18. https://doi.org/10.1016/0377-0273(96)00018-2.

Martin, D., Nokes, R., 1988. Crystal settling in a vigorously convection magma chamber. Nature 332, 534–536.

Mathews, J., Campbell, Q.P., Xu, H., Halleck, P., 2017. A review of the application of X-ray computed tomography to the study of coal. Fuel 209, 10–24. https://doi.org/10.1016/j.fuel.2017.07.079.

McCarter, R.L., Fodor, R.V., Trusdell, F., 2006. Perspectives on basaltic magma crystallization and differentiation: lava-lake blocks erupted at Mauna Loa volcano summit, Hawaii. Lithos 90 (3–4), 187–213. https://doi.org/10.1016/j.lithos.2006.03.005.

McCubbin, F.M., Steele, A., Hauri, E.H., Nekvasil, H., Yamashita, S., Hemley, R.J., 2010. Nominally hydrous magmatism on the moon. Proc. Natl. Acad. Sci. 107 (25), 11223–11228. https://doi.org/10.1073/pnas.100667710.

McCubbin, F.M., Vander Kaaden, K.E., Tartèse, R., Klima, R.L., Liu, Y., Mortimer, J., Barnes, J.J., et al., 2015. Magmatic volatiles (H, C, N, F, S, Cl) in the lunar mantle, crust, and regolith: abundances, distributions, processes, and reservoirs. Am. Mineral. 100, 1668–1707. https://doi.org/10.2138/am-2015-4934ccbyncnd.

McCubbin, F.M., Herd, C.D.K., Yada, T., Hutzler, A., Calaway, M.J., Allton, J.H., Corrigan, C.M., Fries, M.D., Harrington, A.D., McCoy, T.J., Mitchell, J.L., Regberg, A. B., Righter, K., Snead, C.J., Tait, K.T., Zolensky, M.E., Zeigler, R.A., 2019. Advanced curation of astromaterials for planetary science. Space Sci. Rev. 215 (48) https://doi.org/10.1007/s11214-019-0615-9.

McMillan, K., Long, P.E., Cross, R.W., 1989. Vesiculation in Columbia River basalts. See Reidel & Hooper 1989, 157–167.

Meyer, C., 2016. The lunar sample compendium database. Astromater. Res. Explor. Sci. https://curator.jsc.nasa.gov/lunar/lsc/.

Mills, R.D., Simon, J.I., Alexander, C.M.O., Wang, J., Christoffersen, R., Rahman, Z., 2014. Chemical zoning of feldspars in lunar granitoids: Implications for the origins of lunar silicic magmas. In: 45th Lunar and Planetary Science Conference, The Woodlands, Texas, 1547.

Moitra, P., Houghton, B.F., 2021. Porosity-permeability relationships in crystal-rich basalts from Plinian eruptions. Bull. Volcanol. 83, 71. https://doi.org/10.1007/s00445-021-01496-7.

Mongrain, J., Larsen, J.F., King, P.L., 2008. Rapid water exsolution, degassing, and bubble collapse observed experimentally in K-phonolite melts. J. Volcanol. Geotherm. Res. 173 (3–4), 178–184. https://doi.org/10.1016/j.jvolgeores.2008.01.026.

Morgan, D.J., Jerram, D.A., 2006. On estimating crystal shape for crystal size distribution analysis. J. Volcanol. Geotherm. Res. 154, 1–7. https://doi.org/10.1016/j.jvolgeores.2005.09.016.

Murase, R., McBirney, A.T., 1970. Viscosity of lunar lavas. Science 167, 1491–1492.

Neal, C.R., Taylor, L.A., 1992. Petrogenesis of mare basalts: a record of lunar volcanism. Geochim. Cosmochim. Acta 56, 2177–2211. https://doi.org/10.1016/0016-7037(92)90184-K.

Neal, C.R., Donohue, P., Fagan, A.L., O'Sullivan, K., Oshrin, J., Roberts, S., 2015. Distinguishing between basalts produced by endogenic volcanism and impact processes: a non-destructive method using quantitative petrography of lunar basaltic samples. Geochim. Cosmochim. Acta 148, 62–80. https://doi.org/10.1016/j.gca.2014.08.020.

Newcombe, M.E., Beckett, J.R., Baker, M.B., Newman, S., Guan, Y., Eiler, J.M., Stolper, E.M., 2019. Effects of pH2O and fO2 on the diffusion of H-bearing species in lunar basaltic liquid and an iron-free basaltic analog at 1 atm. Geochim. Cosmochim. Acta 259, 316–343. https://doi.org/10.1016/j.gca.2019.05.033.

Nicholis, M.G., Rutherford, M.J., 2009. Graphite oxidation in the Apollo 17 orange glass magma: implications for the generation of a lunar volcanic gas phase. Geochim. Cosmochim. Acta 73 (19), 5905–5917. https://doi.org/10.1016/j.gca.2009.06.022.

Nicolas, A., 1992. Kinematics in magmatic rocks with special reference to Gabbros. J. Petrol. 33 (4), 891–915. https://doi.org/10.1093/petrology/33.4.891.

Nicolas, A., Ildefonse, B., 1996. Flow mechanisms and viscosity in basaltic magma chambers. Geophys. Res. Lett. 23 (16), 2013–2016. https://doi.org/10.1029/96GL02073.

Object Research Systems (ORS) Inc, 2020. Dragonfly 2020.2 [Computer software]. Montreal, Canada. software available at. http://www.theobjects.com/dragonfly.

Okamura, S., Nakamura, M., Takeuchi, S., Tsuchiyama, A., Nakano, T., Uesugi, K., 2009. Magma deformation may induce non-explosive volcanism via degassing through bubble networks. Earth Planet. Sci. Lett. 281, 267–274. https://doi.org/10.1016/j.epsl.2009.02.036.

Papike, J.J., Hodges, F.N., Bence, A.E., Cameron, M., Rhodes, J.M., 1976. Mare basalts: crystal chemistry, mineralogy, and petrology. Rev. Geophys. Space Phys. 14 (4), 475–540.

Papike, J., Taylor, L., Simon, S., 1991. Lunar minerals. In: Heiken, G.H., Vaniman, D.T., French, B.M. (Eds.), The Lunar Source Book: A User's Guide to the Moon. Cambridge University Press, Cambridge, pp. 121–161.

Passey, S.R., Bell, B.R., 2007. Morphologies and emplacement mechanisms of the lava flows of the Faroe Islands Basalt Group, Faroe Islands, NE Atlantic Ocean. Bull. Volcanol. 70, 139–156. https://doi.org/10.1007/s00445-007-0125-6.

Paterson, S.R., Fowler Jr., T.K., Schmidt, K.L., Yoshinobu, A.S., Yuan, E.S., Miller, R.B., 1998. Interpreting magmatic fabric patterns in plutons. Lithos 44, 53–82. https://doi.org/10.1016/S0024-4937(98)00022-X.

Paterson, S.R., Ardill, K., Vernon, R., Zak, J., 2019. A review of mesoscopic magmatic structures and their potential for evaluating hypersolidus evolution of intrusive complexes. J. Struct. Geol. 125, 134–147. https://doi.org/10.1016/j.jsg.2018.04.022.

Polacci, M., Papale, P., 1997. The evolution of lava flows from ephemeral vents at Mount Etna: insights from vesicle distribution and morphological studies. J. Volcanol. Geotherm. Res. 76 (1–2), 1–17. https://doi.org/10.1016/S0377-0273(96)00070-4.

Potts, N.J., Bromiley, G.D., Brooker, R.A., 2021. An experimental investigation of F, Cl and H2O mineral- melt partitioning in a reduced, model lunar system. Geochim. Cosmochim. Acta 294, 232–254. https://doi.org/10.1016/j.gca.2020.12.003.

Qian, Y., Xiao, L., Wang, Q., Head, J.W., Yang, R., Kang, Y., van der Bogert, C.H., Hiesinger, H., Lai, X., Wang, G., Pang, Y., Zhang, N., Yuan, Y., He, Q., Huang, J., Zhao, J., Wang, J., Zhao, S., 2021. China's Chang'e-5 landing site: geology, stratigraphy, and provenance of materials. Earth Planet. Sci. Lett. 561, 116855 https://doi.org/10.1016/j.epsl.2021.116855.

Rai, N., Perrillat, J.-P., Mezouar, M., Colin, A., Petitgirard, S., van Westrenen, W., 2019. *In situ* viscometry of primitive lunar magmas at high pressure and high temperature. Front. Earth Sci. 30 https://doi.org/10.3389/feart.2019.00094.

Rhodes, J.M., Hubbard, N.J., 1973. Chemistry, classification, and petrogenesis of Apollo 15 mare basalts. In: Proceedings of the Fourth Lunar Science Conference, 2, pp. 1127–1148.
Roberts, C.E., Gregg, T.K.P., 2019. Rima Marius, the moon: formation of lunar sinuous rilles by constructional and erosional processes. Icarus 317, 682–688. https://doi.org/10.1016/j.icarus.2018.02.033.
Rowland, S.K., Walker, G.P.L., 1988. Mafic-crystal distributions, viscosities, and lava structures of some Hawaiian lava flows. J. Volcanol. Geotherm. Res. 35, 55–66. https://doi.org/10.1016/0377-0273(88)90005-4.
Rowland, S.K., Walker, G.P.L., 1990. Pahoehoe and aa in Hawaii: volumetric flow rate controls the lava structure. Bull. Volcanol. 52, 615–628. https://doi.org/10.1007/BF00301212.
Rumpf, M.E., Needham, H., Fagents, S.A., 2020. Thicknesses of lava flows in satellite images: comparison of layered mare units with terrestrial analogs. Icarus 350, 113853. https://doi.org/10.1016/j.icarus.2020.113853.
Ryder, G., 1985. Catalog of Apollo 15 Rocks. Part 1. National Aeronautics and Space Administration Johnson Space Center Contribution 20787.
Ryder, G., 1993. Catalog of Apollo 17 Rocks. National Aeronautics and Space Administration Johnson Space Center Contribution #26088, p. 1.
Saal, A.E., Hauri, E.H., Cascio, M.L., Van Orman, J.A., Rutherford, M.C., Cooper, R.F., 2008. Volatile content of lunar volcanic glasses and the presence of water in the Moon's interior. Nat. Lett. 454, 192–195. https://doi.org/10.1038/nature07047.
Sato, M., 1979. The driving mechanism of lunar pyroclastic eruptions inferred from the oxygen fugacity behavior of Apollo 17 orange glass. In: Proceedings of the 10th Lunar and Planetary Science Conference, Houston, Texas, pp. 311–325.
Schneider, C.A., Rasband, W.S., Eliceiri, K.W., 2012. NIH image to ImageJ: 25 years of image analysis. Nat. Methods 9 (7), 671–675. https://doi.org/10.1038/nmeth.2089.
Self, S., Keszthelyi, L.P., Thordarson, T., 1998. The importance of Pāhoehoe. Annu. Rev. Earth Planet. Sci. 26, 81–110.
Shaw, H., 1969. Rheology of basalt in the melting range. J. Petrol. 10, 510–535.
Shea, T., Houghton, B.F., Gurioli, L., Cashman, K.V., Hammer, J.E., Hobden, B.J., 2010. Textural studies of vesicles in volcanic rocks: an integrated methodology. J. Volcanol. Geotherm. Res. 190, 271–289. https://doi.org/10.1016/j.jvolgeores.2009.12.003.
Shearer, C.K., Hess, P.C., Wieczorek, M.A., Pritchard, M.E., Parmentier, E.M., Borg, L.E., Longhi, J., Elkins-Tanton, L.T., Neal, C.R., Antonenko, I., Canup, R.M., Halliday, A. N., Grove, T.L., Hager, B.H., Lee, D.-C., Wiechert, U., 2006. Thermal and magmatic evolution of the moon. In: Jollif, B.L., Wieczorek, M.A., Shearer, C.K., Neal, C.R. (Eds.), New Views of the Moon. Reviews in Mineralogy & Geochemistry, 60(1), pp. 365–518. https://doi.org/10.2138/rmg.2006.60.4.
Sok, R., Varslot, T.K., Ghous, A., Latham, S., Sheppard, A.P., Knackerstedt, M., 2009. Pore scale characterization of carbonates at multiple scales: integration of micro-CT, BSEM, and FIBSEM. Petrophysics 51 (6).
Spudis, P.D., Swann, G.A., Greeley, R., 1988. The formation of Hadley Rille and implications for the geology of the Apollo 15 region. In: Proceedings of the Lunar Planetary Science Conference, 18, pp. 243–254.
Swann, G.A., et al., 1972. Preliminary geologic investigation of the Apollo 15 landing site. In: Apollo 15: Preliminary Science Report. NASA SP-289, pp. 21–31.
Takeda, H., Miyamoto, M., Ishii, T., Lofgren, G.E., 1975. Relative cooling rates of mare basalts at the Apollo 12 and 15 sites as estimated from pyroxene exsolution data. In: Proceedings of the 6th Lunar Science Conference, pp. 987–998.
Tartèse, R., Anand, M., Barnes, J.J., Starkey, N.A., Franchi, I.A., Sano, Y., 2013. The abundance, distribution, and isotopic composition of hydrogen in the moon as revealed by basaltic lunar samples: implications for the volatile inventory of the moon. Geochim. Cosmochim. Acta 122, 58–74. https://doi.org/10.1016/j.gca.2013.08.014.
Tartèse, R., Anand, M., Joy, K.H., Franchi, I.A., 2014. H and Cl isotope systematics of apatite in brecciated lunar meteorites Northwest Africa 4472, Northwest Africa 773, Sayh al Uhaymir 169, and Kalahari 009. Meteorit. Planet. Sci. 49 (12), 2266–2289. https://doi.org/10.1111/maps.12398.
Taylor, S.R., 1982. Planetary Science: A Lunar Perspective. Publishers Production International, Houston, Texas, 481 p.
Taylor, G.J., Warren, P.H., Ryder, G.C., Delano, J.W., Pieters, C.M., Lofgren, G.W., 1991. Lunar rocks. In: Heiken, G.H., Vaniman, D.T., French, B.M. (Eds.), The Lunar Source Book: A User's Guide to the Moon. Cambridge University Press, Cambridge, pp. 183–284.
Thordarson, T., 1995. Volatile Release and Atmospheric Effects of Basaltic Fissure Eruptions. Ph.D. thesis. University of Hawaii, Manoa, Honolulu, 580 pp.
Tolometti, G.D., Neish, C.D., Osinski, G.R., Hughes, S.S., Kobs Nawotniak, S.E., 2020. Interpretations of lava flow properties from radar remote sensing data. Planet. Space Sci. 190, 104991 https://doi.org/10.1016/j.pss.2020.104991.
Treiman, A.H., Drake, M.J., 1983. Origin of lunar meteorite ALHA 81005: clues from the presence of terrae clasts and a very low-titanium mare basalt clast. Geophys. Res. Lett. 10 (9), 783–786. https://doi.org/10.1029/GL010i009p00783.
Vaniman, D.T., Reedy, R., Heiken, G.H., Olhoeft, G., Mendell, W.W., 1991. The lunar environment. In: Heiken, G.H., Vaniman, D.T., French, B.M. (Eds.), The Lunar Source Book: A User's Guide to the Moon. Cambridge University Press, Cambridge, pp. 27–60.
Vásárhelyi, L., Kónya, Z., Kukovecz, Á., Vajtai, R., 2020. Microcomputed tomography-based characterization of advanced materials: a review. Mater. Today Adv. 8, 100084 https://doi.org/10.1016/j.mtadv.2020.100084.
Vernon, R.H., 2018. A Practical Guide to Rock Microstructure, 2nd edition. Cambridge University Press, Cambridge. https://doi.org/10.1017/9781108654609.
Vye-Brown, C., Self, S., Barry, T.L., 2013. Architecture and emplacement of flood basalt flow fields: case studies from the Columbia River Basalt Group. NW USA Bull. Volcanol. 75, 697. https://doi.org/10.1007/s00445-013-0697-2.
Walker, D., Longhi, J., Stolper, E.M., Grove, T.L., Hays, J.F., 1975. Origin of titaniferous lunar basalts. Geochim. Cosmochim. Acta 39 (9), 1219–1235. https://doi.org/10.1016/0016-7037(75)90129-5.
Wang, Y., Miller, J.D., 2020. Current developments and applications of micro-CT for the 3D analysis of multiphase mineral systems in geometallurgy. Earth Sci. Rev. 211, 103406 https://doi.org/10.1016/j.earscirev.2020.103406.
Warner, J., 1970. Apollo 12 Lunar-Sample Information. National Aeronautics and Space Administration Technical Report R-353.
Weider, S.Z., Crawford, I.A., Joy, K.H., 2010. Individual lava flow thicknesses in Oceanus Procellarum and Mare Serenitatis determined from Clementine multi-spectral data. Icarus 209, 323–336.
Wetzel, D.T., Hauri, E.H., Saal, A.E., 2015. Carbon content and degassing history of the lunar volcanic glasses. Nat. Geosci. 8, 755–758. https://doi.org/10.1038/ngeo2511.
Whitford-Stark, J.J., 1982. Factors influencing the morphology of volcanic landforms: and earth-moon comparison. Earth-Sci. Rev. 18, 109–168.
Wilmoth, R.A., Walker, G.P.L., 1993. P-type and S-type pahoehoe: a study of vesicle distribution patterns in Hawaiian lava flows. J. Volcanol. Geotherm. Res. 55, 129–142.
Wilson, L., 2009. Volcanism in the solar system. Nat. Geosci. 2, 389–397. https://doi.org/10.1038/ngeo529.
Wilson, L., Head, J.W., 1981. Ascent and eruption of basaltic magma on the earth and moon. J. Geophys. Res. 86, 2971–3001.
Wilson, L., Head, J.W., 2018. Controls on lunar basaltic volcanic eruption structure and morphology: gas release patterns in sequential eruption phases. Geophys. Res. Lett. 45 (12), 5852–5859. https://doi.org/10.1029/2018GL078327.
Woodcock, N.H., Naylor, M.A., 1983. Randomness testing in three-dimensional orientation data. J. Struct. Geol. 5, 539–548.
Wu, X., Schepartz, L.A., 2009. Application of computed tomography in paleoanthropological research. Prog. Nat. Sci. 19 (8), 913–921. https://doi.org/10.1016/j.pnsc.2008.10.009.
Žák, J., Patterson, S.R., Memeti, V., 2007. Four magmatic fabrics in the Tuolumne batholith, central Sierra Nevada, California (USA): implications for interpreting fabric patterns in plutons and evolution of magma chambers in the upper crust. Geol. Soc. Am. Bull. 119, 184–201. https://doi.org/10.1130/B25773.1.
Zeigler, R.A., Eckley, S.A., Hanna, R., Edey, D., Ketcham, R.A., Gross, J., McCubbin, F.M., 2021. Using X-Ray Computed Tomography to Image Apollo Drive Tube 73002. Lunar and Planetary Science Conference LII, Abstract #2632.
Zhang, P., Lee, Y.I., Zhang, J., 2019. A review of high-resolution X-ray computed tomography applied to petroleum geology and a case study. Micron 124, 102702. https://doi.org/10.1016/j.micron.2019.102702.
Zolensky, M., Mikouchi, T., Fries, M., Bodnar, R., Jenniskens, P., Yin, Q.-Z., Hagiya, K., Ohsumi, K., Komatsu, M., Colbert, M., Hanna, R., Maisano, J., Ketcham, R., Kebukawa, Y., Nakamura, T., Matsuoka, M., Sasaki, S., Tsuchiyama, A., Gounelle, M., Le, L., Martinez, J., Ross, K., Rahman, Z., 2014. Mineralogy and petrography of C asteroid regolith: the Sutter's mill CM meteorite. Meteorit. Planet. Sci. 49, 1997–2016. https://doi.org/10.1111/maps.12386.